# Structural study on the microtubule-binding domain of axonemal dynein

A Doctoral Thesis
By
Akiyuki Toda

Submitted to Graduate School of Science,
Osaka University
Japan

February, 2020

# Acknowledgement

This study has been carried out under the direction of Professor Genji Kurisu of Institute for Protein Research, Osaka University. I would like to express the deepest appreciation to him for incessant guidance and encouragement throughout this work.

I am grateful to Dr. Yosuke Nishikawa of Daiichi Sankyo RD Novare Co., Ltd. for appropriate advice and support about experiments.

I am deeply grateful to Professor Atsushi Nakagawa of Institute for Protein Research, Osaka University, Professor Yoshie Harada of Institute for Protein Research, Professor Takahide Kon of Osaka University, and Associate Professor Hideaki Tanaka of Institute for Protein Research, Osaka University for reviewing manuscript and appropriate advice.

I am also deeply grateful to the staff of BL44XU at SPring-8 for support with X-ray data collection.

I appreciate the financial support by Grand-in-Aid for Research Fellows of the Japan Society for the Promotion of Science (17J07553).

Finally, I would like to thank my family for their constant support and encouragements.

戸田 暁之

Akiyuki Toda

February, 2020

## Table of contents


## Chapter 1

## Introduction

1.1 Molecular motors

1.2 Dyniens

1.3 Characteristic insertion in several MTBDs of axonemal dynein

1.4 Axonemal dynein light chain-1

1.5 Purpose of this study

## Chapter 2

## Structure-function relationship of the axonemal dynein light chain-1

2.1 Introduction

2.2 Materials and Methods

2.3 Results

2.4 Discussion

## Chapter 3

## Structural analysis of LC1-MTBD complex

3.1 Introduction

3.2 Materials and Methods

3.3 Results

3.4 Discussion

## Chapter 4

## X-ray crystallographic analysis of IAD (DNAH10) MTBD

4.1 Introduction

4.2 Materials and Methods

4.3 Results

4.4 Discussion

## Chapter 5

## Conclusion

## References

## List of publications

## Abbreviation

| | |
|---|---|
| $AAA^+$ | ATPase associated with diverse cellular activities |
| AC | Artificial coiled coil |
| ATP | ATPase associated with diverse cellular activities |
| BL | Beam line |
| CC | Coiled coil |
| CTT | C-terminal tail |
| DLS | Dynamic light scattering |
| DTT | Dithiothreitol |
| EM | Electron microscopy |
| ET | Electron tomography |
| GST | Glutathione S-transferase |
| HC | Heavy chain |
| IAD | Inner arm dynein |
| IC | Intermediate chain |
| IPTG | Isopropyl β-D-1-thiogalactopyranoside |
| LB | Luria-Bertani |
| LC | Light chain |
| LC1 | axonemal dynein light chain-1 |
| LIC | Light intermediate chain |

| | |
|---|---|
| LRR | Leucine-rich repeat |
| MR | Molecular replacement |
| MT | Microtubule |
| MTBD | Microtubule-binding domain |
| NMR | Nuclear magnetic resonance |
| OAD | Outer arm dynein |
| PAGE | Polyacrylamide gel electrophoresis |
| PMSF | Phenylmethylsulfonyl fluoride |
| PDB | Protein Data Bank |
| PEG | Polyethylene glycol |
| RMSD | Root mean square deviation |
| SAD | Single-wavelength anomalous dispersion |
| SDS | Sodium dodecyl sulfate |
| SeMet | Seleno-L-methionine |
| Tris | Tris (hydroxymethyl) aminomethane |
| SPring-8 | Super Photon Ring-8 |

# Chapter 1

# General introduction

## 1.1 Molecular motors

In eukaryotic cells, molecular motors are involved in various biological functions, such as mitosis, intracellular transport, cilia/flagella movement. Among the molecular motors, three major motor proteins have been well studied; myosin, kinesin, and dynein (1). Myosins move along actin filaments while kinesins and dyneins move on the microtubule filaments (2). In order to move on the cytoskeletal tracks, they need to produce power force converted from ATP hydrolysis. Dyneins are very unique compared with other myosin and kinesin, because their functional domains are structurally separated as independent functional domains and dyneins work as the large supramolecular complexes (> 1 MDa) (1).

## 1.2 Dyneins

### 1.2.1 Cytoplasmic and axonemal dyneins

Dyniens are microtubule (MT)-based molecular motors that move along microtubules toward the minus end, and drive diverse biological functions (3). They work as a large multiple complex (> 1 MDa) consisting of heavy chain (HC), intermediate chain (IC), light-intermediate chain (LIC), and light chain (LC) (Figure 1.1). Dyneins are

divided into two groups, cytoplasmic and axonemal dyniens, in terms of their physiological functions. A cytoplasmic dynein is involved in intracellular transport and cell mitosis, while an axonemal dynein produces the driving power for ciliary/flagellar beating. The axoneme of the cilia/flagella has the 9+2 structure, nine doublet microtubules surrounding central two microtubules (4, 5). Axonemal dyneins are regularly arranged within the axoneme, and subdivided into two sub-groups based on their location: dyneins located on the outer side of the axoneme are called Outer Arm Dynein (OAD), while those on the inner side are Inner Arm Dynein (IAD) (Figure 1.2).

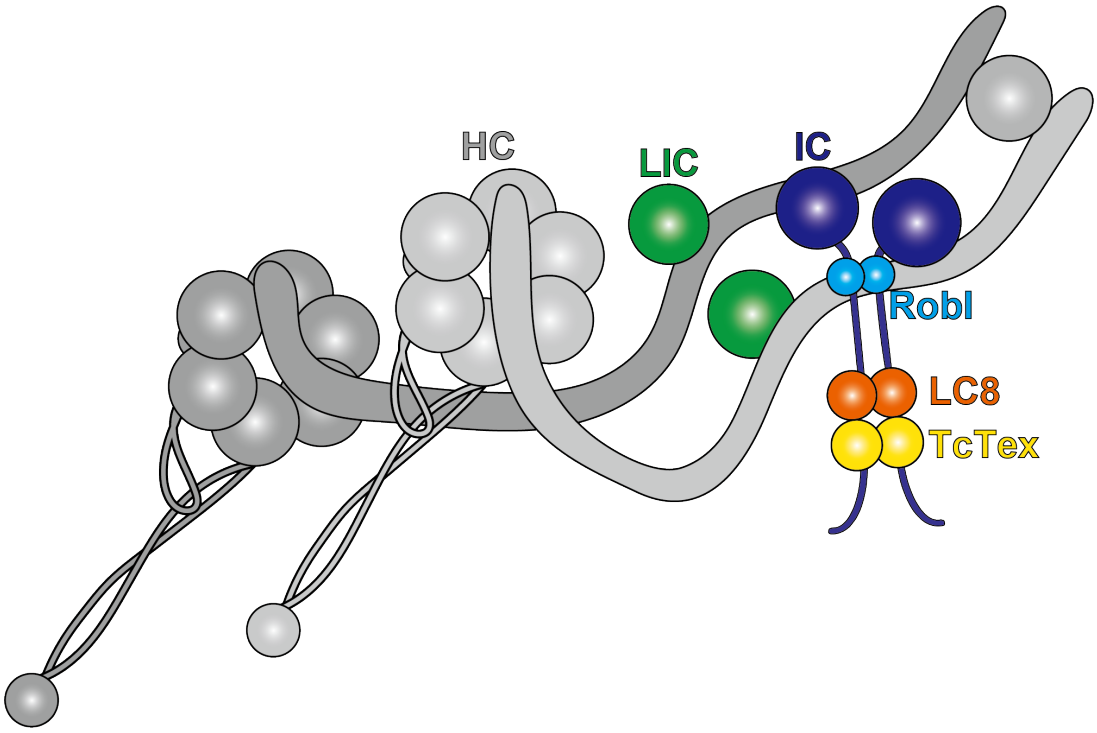


**Figure 1.1 Architecture of cytoplasmic dynein**

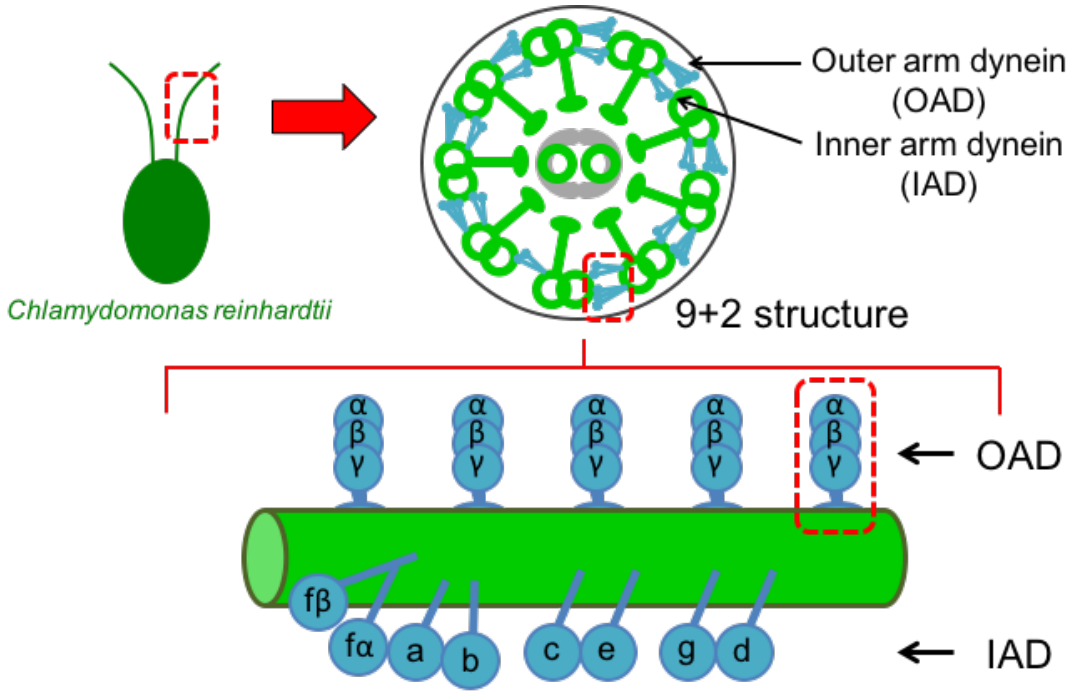


**Figure 1.2 Schematic diagram of axoneme and axonemal dyneins**

### 1.2.2 Architecture of dyneins

The structural analysis of dynein motor began with the LCs which have relatively smaller molecular weights and then progressed to the larger chains. The first structural report on dynein HC, which possesses ATPase and motor activity, was the negatively stained electron microscopic study of dynein-c purified from *Chlamydomonas reinhardtii* (6). Although the resolution of this 1$^{st}$ structural study by electron microscopy (EM) was too low to build the atomic model, the higher resolution structural models of the cytoplasmic dynein motor domains were determined later by X-ray crystallography and cryo-EM (7–13). These atomistic structural studies revealed that the dynein HC is

spatially separated by several functional units, such as the N-terminal tail, linker, $AAA^+$ ring (ATPase associated with various cellular activities ring), stalk, the microtubule binding domain (MTBD), strut/buttress, and C-sequence (Figure 1.3). As compared with structural studies of cytoplasmic dynein, only two atomic structures of HC that only comprise MTBD are available in Protein Data Bank (PDB) (14, 15). Therefore, the molecular mechanism underlying the motor activities of axonemal dynein remains relatively unclear.

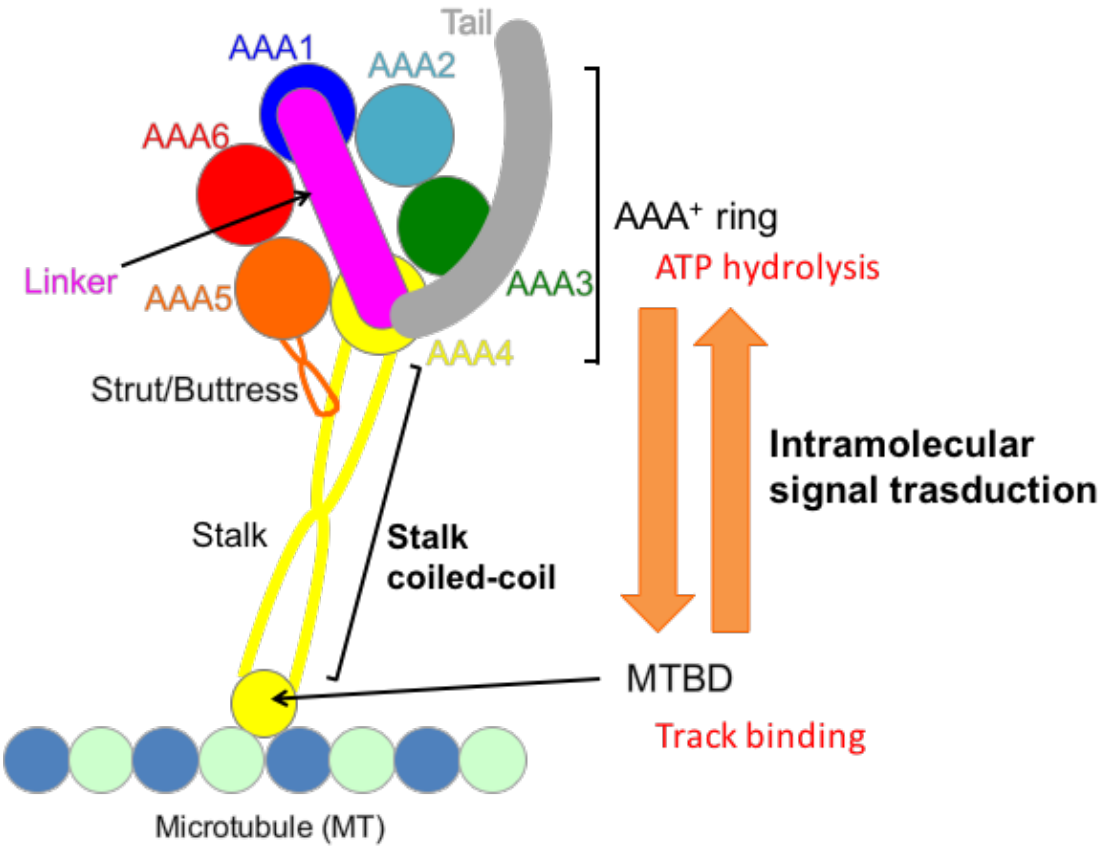


**Figure 1.3 Schematic diagram of dynein heavy chain and its intramolecular communication**

### 1.2.3 Helix sliding model

To move along a microtubule, the communication between ATP hydrolysis in the AAA+ ring and microtubule binding at the MTBD must be properly coupled. However, the AAA+ ring and the MTBD are structurally separated about 15 nm by the long coiled coil structure of the stalk region (Figure 1.3). This long range intramolecular communication is currently explained by the helix sliding model, whereby a registry change occurs between two helices in the coiled-coil region of the stalk (16–18). In this model, the coiled coil packing of the stalk region is thought to be switched between two structural conformations, named the α- and β-registries (Figure 1.4), corresponding to the high and low affinities of the MTBD for the microtubules. Indeed, the microtubule co-sedimentation assays have confirmed that the α- and β-registory in both cytoplasmic and axonemal dyneins show a high and low microtubule-binding affinity, respectively (14, 16).

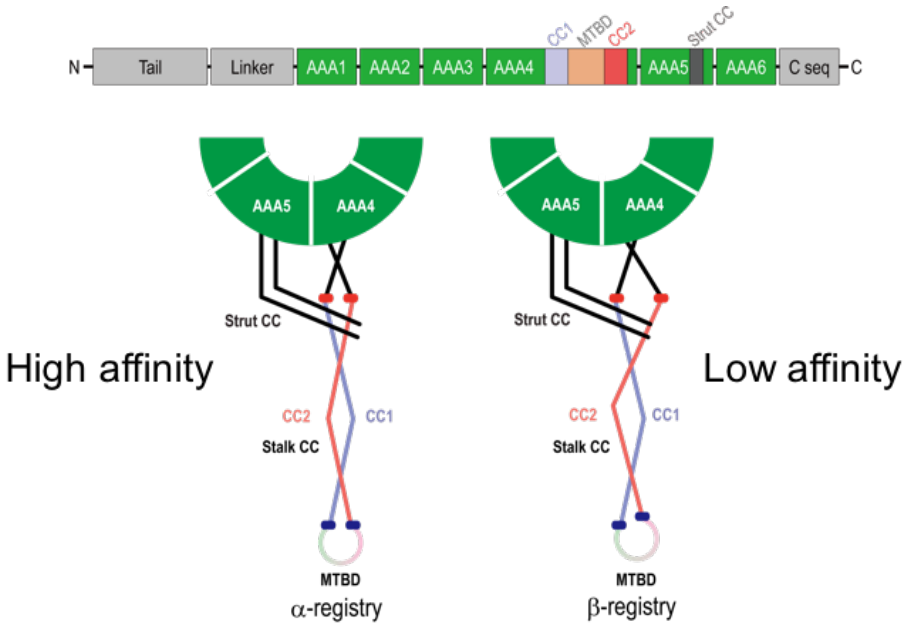

**Figure 1.4 Helix sliding model**

This figure is modified from the figure 1 of (18).

### 1.2.4 Motor cycle of dynein

To understand motor cycle of dynein, many structural (6–13, 18–21) and biochemical studies (17, 22, 23) has been performed. According to these results, at present, motor cycle of dynein is considered as follows (Figure 1.5) (24, 25); (I) When the AAA1 site is empty, the dynein is attached to the MT. (II) ATP binding to the AAA1 induces detachment of the MT and the linker bending. (III) ATP bound to the AAA1 is hydrolyzed and phosphate is released. (IV) The dynein rebinds to the MT, and (V) it leads the straightening of the linker (power stroke). This model has been demonstrated by many studies of cytoplasmic dynein. It is considered that motor cycle of axonemal dynein is mostly similar to that of cytoplasmic dynein.

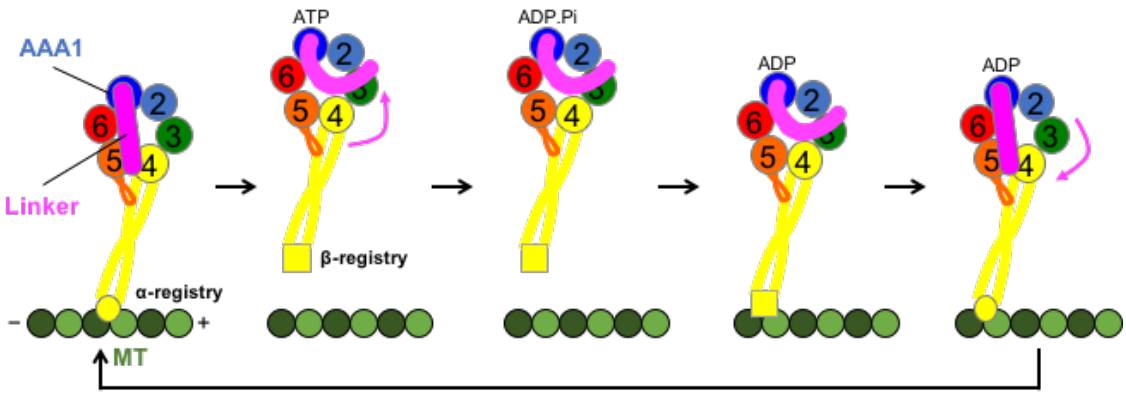


**Figure 1.5 Model for mechanochemical cycle of dynein**

### 1.2.4 Axonemal dynein

Genome analyses of several organisms have revealed that there are at least 15 HC genes present in most eukaryote; two of which encode cytoplasmic dyneins, while the others encode axonemal dyneins. Cytoplasmic dyneins work a dimer, whereas the physiological oligomeric state of functional axonemal dynein HCs vary from a monomer, a dimer, and a trimer. Moreover, the MT gliding assays have revealed that some axonemal dyneins display a clockwise translocation of MTs (26, 27). These findings indicate that axonemal dyneins are diverse in terms of the functional properties of their HCs. Despite the fact that the axonemal dyneins were characterized uniquely compared to the cytoplasmic dyneins, an EM images showed that the architecture of axonemal dynein HC is quite similar to that of cytoplasmic dynein (6). In cilium/flagellum, axonemal dyneins need to respond to curvature of microtubules accompanied with beating to work precisely (28). There are many axonemal dynein HCs (e.g. fourteen in human) which are periodically aligned in the axoneme (5, 29). A cryo-electron tomographic (ET) study had demonstrated that axonemal dyneins showed their different activity states in flagellum corresponding to the microtubule bending (30). However, it remains unclear why these different motor properties between axonemal and cytoplasmic dyneins are attributed and what the functional role of each specific axonemal dynein is.

## 1.3 Characteristic insertion in several MTBDs of axonemal dynein

In several axonemal dyneins (IADa, b, c, d, e, and OADγ in *Chlamydomonas*), there is a characteristic insertion in MTBD. It is called a flap region which consists of 11-16 amino acids and forms a β-hairpin structure (Figure 1.6) (14). A cryo-EM study had indicated that the flap of DNAH7 (IADa in human) is able to interact with the protofilament adjacent to the filament to which the MTBD was bound (15). The functional role of the flap is still unclear.

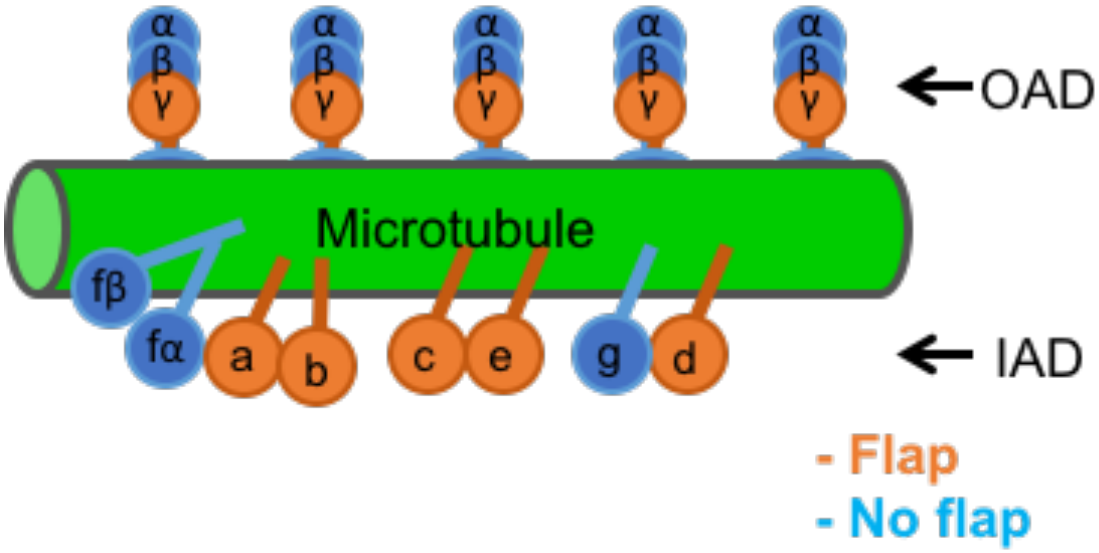


**Figure 1.6 Distribution of axonemal dyneins which possess the flap**

Schematic view of the positions of the HCs in the 96 nm repeat. Colours of the HCs correspond to whether they possess a flap (orange) or not (cyan).

## 1.4 Axonemal dynein light chain-1

In axonemal dyneins, the outer arm dynein (OAD) complex, which produces the main driving force for ciliary/flagellar beating (31), comprises three heavy chains (α, β, and γ) and other accessory components (32, 33). It is known that the mutations in the heavy chain component including the CC2 helix of human DNAH5-MTBD, which corresponds to OADγ in *Chlamydomonas reinhardtii*, cause ciliopathies in human (34). As shown in Figure 1.1, most of the dynein accessory chains are thought to be bound to the N-terminal tail region of the dynein heavy chain. Similarly to the other light chains, the axonemal dynein light chain-1 (LC1) from *Chlamydomonas reinhardtii* had been assumed to be bound to the $AAA^+$ ring of the OADγ heavy chain (OADγ) (35, 36). Recently, however, it was reconsidered that LC1 interacts with the MTBD of OADγ (Figure 1.7) (37).

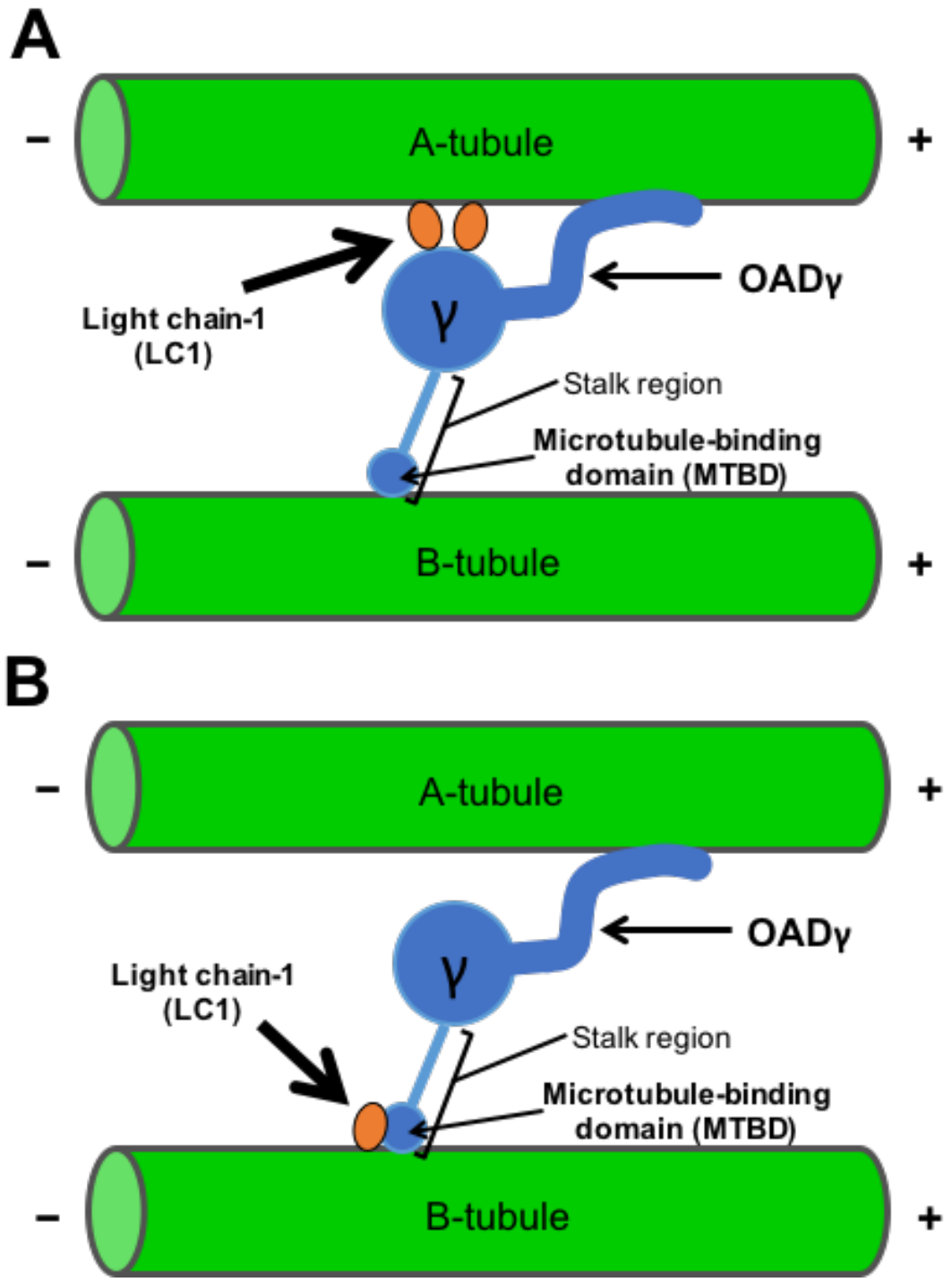


**Figure 1.7 Previous and current models of localization of LC1 in axoneme**

(A) Previous model of LC1 binding to the OADγ

(B) Current model of LC1 binding to the OADγ

A mutational study on LC1 have shown that expression of LC1 mutants lead to dominant-negative effects on swimming velocity and beat frequency in *Chlamydomonas reinhardtii* (38), and that knockdown of LC1 leads to low beat frequency in planaria (39). LC1 is also highly conserved in vertebrates (e.g. DNAL1 in *Homo sapiens*), and mutations of LC1 cause primary ciliary dyskinesia (40, 41). Furthermore, a microtubule co-sedimentation assay has suggested that LC1 is able to bind to the microtubule with low affinity (35). These studies clearly show that LC1 possesses unique characteristics among the other light chains and also that LC1 is important for regulation of precise ciliary/flagellar beating.

From a structural point of view, there are two reports on LC1 structures determined by NMR spectroscopy (42, 43). The NMR structures of LC1 displays an unique leucine-rich repeat (LRR) structure, as expected from the amino acid sequences of LC1.

## 1.5 Purpose of this study

Many biochemical and structural analyses about dyneins have been performed until now. However, the structural studies are heavily biased onto cytoplasmic dyneins and less structural studies on axonemal dyneins. It is still unclear what kind of factors contribute to unique molecular motor properties of axonemal dyneins obviously different

from those of cytoplasmic dyneins. Thus, I focused on three topics concerning about the structures of axonemal dyneins especially on the stalk/MTBD region: (i) the structure-function relationship of LC1, (ii) the complex formation of LC1 and MTBD of OADγ, and (iii) the structural diversity of MTBD in axonemal dyneins revealed by the new structure of DNAH10 stalk. This study sheds light on not only the structure-function relationship of LC1/MTBD but also the unique motor properties specific to axonemal dyneins.

# Chapter 2

# Structure-function relationship of the axonemal dynein light chain-1

## 2.1 Introduction

As described in Chapter 1, LC1 is a highly conserved regulatory protein of the OAD complex. Based on the previous structural study of LC1 by NMR spectroscopy, LC1 showed a flexible conformation. Although NMR structures of LC1 are available (42, 43), the resolution of the LC1 structure is not high enough to discuss about the molecular mechanism at the atomic level. Therefore, I independently determined the X-ray structure of LC1 at 1.55 Å resolution to enable more detailed discussions.

## 2.2 Materials and Methods

### 2.2.1 Construct

The plasmid of LC1 was kindly provided from Professor Toshiki Yagi of Prefectural University of Hiroshima. The plasmid was pGEX6P2 which was inserted LC1 gene from *Chlamydomonas reinhardtii* (Uniprot KB: Q9XHH2, 1-198aa) between BamHI and EcoRI sites (Figure 2.1).

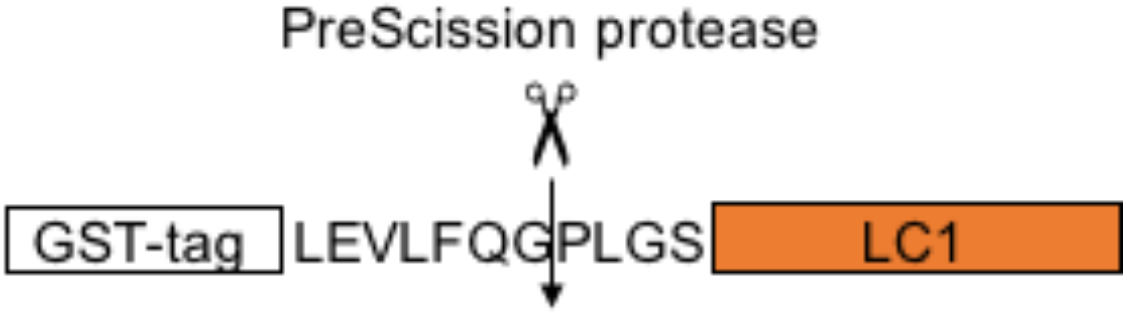


**Figure 2.1 Design of construct of GST-tagged LC1**

### 2.2.2 Expression and purification

The plasmid was transformed into BL21(DE3) strain. Cells were cultured in 6 mL of LB medium supplemented with 100 μg/mL ampicillin at 37 ºC. The cultured cells were transferred to 1 L of LB medium and cultured at 37 ºC until the optical density $OD_{600}$ reached ~0.5. The cells were cultured for 20 h after the temperature was lowered to 20 ºC and 0.1 mM isopropyl-1-thio-galactopyranoside (IPTG) was added for induction. The cells were then harvested by centrifugation and stored at -80 ºC. The frozen cells from 2 L culture were resuspended with 20 mL of buffer A (50 mM Tris-HCl pH 8.0, 100 mM NaCl) supplemented with 1 mM benzamidine hydrochloride and 1 mM 6-aminocaproic acid per 1 L culture, and lysed by two passages through a French press. The lysate was clarified by ultracentrifugation at 200,000 g for 30 min., and the supernatant was mixed with 8 mL of Glutathione Sepharose 4B (GE Healthcare) resin and then incubated for 30

min. The resin was washed with 5 column volumes of buffer A supplemented with 1 mM DTT three times, and then packed into a column. After washing the resin, 2 mL of buffer A supplemented with 1 mM DTT and 100 units of Precission Protease (GE Healthcare) were added to the resin, and then incubated at 4 ºC for overnight. The protein was eluted with buffer A. The eluted sample was loaded onto a Superdex 200 16/600 (GE Healthcare) equilibrated in buffer B (10 mM Tris-HCl pH 8.0, 100 mM NaCl). Fractions containing LC1 were collected, and passed through 4 mL of Glutathione Sepharose 4B (GE Healthcare) to remove residual GST. Finally, the LC1 sample was concentrated to 20 mg/mL, and stored at -80 ºC.

### 2.2.3 Crystallization and data collection

LC1 crystals were grown at 4 ºC with the sitting-drop vapor-diffusion method by mixing 200 nL of LC1 (20 mg/mL protein in buffer B) with an equal volume of reservoir solution (0.1 M Ammonium phosphate monobasic, 10% (w/v) PEG3350). LC1 crystals were soaked in cryo-protectant solution (0.1 M Ammonium phosphate monobasic, 35% (w/v) PEG3350, 10 mM Tris-HCl pH 8.0, 100 mM NaCl) for overnight, and then flash-cooled in liquid nitrogen. X-ray diffraction experiment was performed at the BL44XU beam line, SPring-8.

### 2.2.4 Structure determination

The collected images were processed using HKL2000 software (44). Molecular replacement and refinement were performed using BALBES (45) and COOT (46),

respectively. TLS parameters were analyzed with the TLSMD server (47), and twelve TLS groups were introduced in the subsequent refinement. The final structure was validated using MolProbity (48). Crystallographic data and refinement statistics are shown in Table 2.1. The coordinates and structure factors for LC1 have been deposited to the worldwide Protein Data Bank (wwPDB) under accession number 5YXM.

## 2.3 Results

### 2.3.1 Overall structure of LC1

I successfully purified LC1 by two steps of GST-affinity and gel-filtration chromatography (Figure 2.2). As a result of initial screening, good-looking crystals were observed in a condition containing 0.1 M Ammonium phosphate monobasic and 10% (w/v) PEG3350 (Figure 2.3). Then, I collected the X-ray diffraction data from a single crystal (Figure 2.4). Finally, I determined the crystal structure of LC1 at 1.55 Å resolution (Figure 2.5 A, Table 2.1). As expected from the sequence and the NMR structures of LC1 (42, 43), the crystal structure of LC1 showed a typical leucine-rich repeat (LRR) conformation. However, large conformational differences between X-ray and NMR structures were found especially in the N- and C- terminus region, and the crystal structure was clearly different from the NMR structures in secondary structure level (Figure 2.5 B, Figure 2.6). In particular, one α helix extending from Asn150 of the crystal structure (lower left corner of Figure 2.5 B) was largely protruded to the outer side. There is a report that Asn150 of DNAL1, which is homologous to LC1 in human, is substituted to Serine in some patients of primary ciliary dyskinesia (PCD) (40). Moreover, it has been also reported that the mutation of N150S reduces the stability of DNAL1 and damages its interactions with the OADγ heavy chains (DNAH5 and DNAH8 in human) and with tubulin (40). Asn150 is one of the consensus sequences of LRR and conserved in various species. These results and reports imply that Asn150 maintains the LRR conformation properly for target binding and also may regulate its binding affinity for the OADγ HC *via* the flexible positioning of an α helix starting from Asn150.

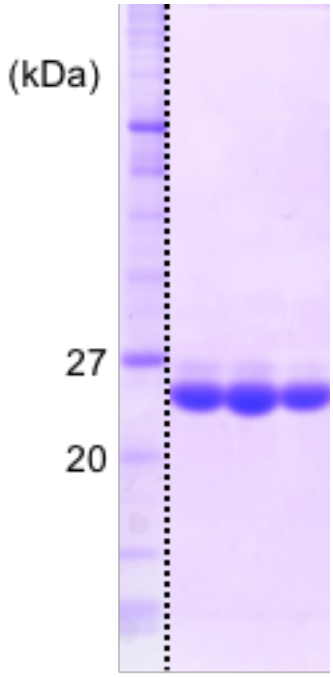


**Figure 2.2 SDS-PAGE of pooled fractions of LC1 in gel-filtration chromatography**

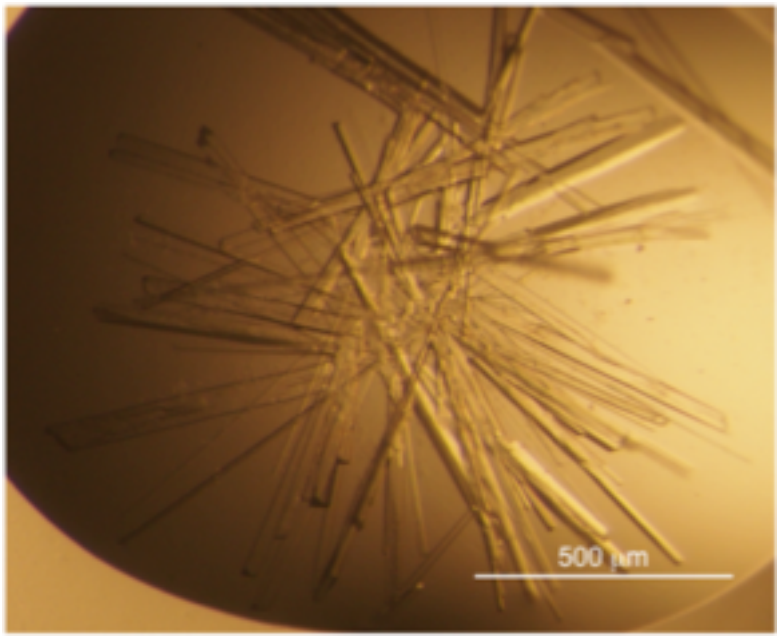


**Figure 2.3 Photo of LC1 crystals**

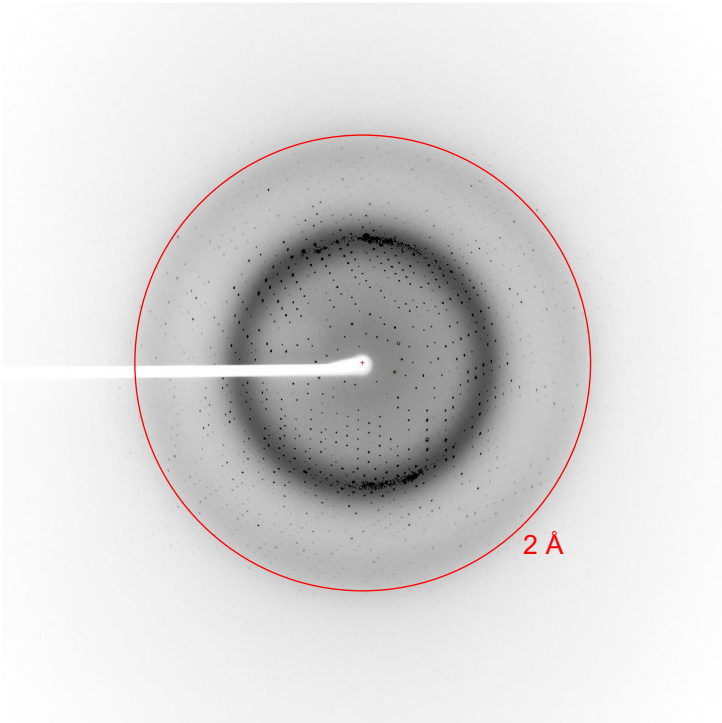


**Figure 2.4 X-ray diffraction pattern of the LC1 crystal**

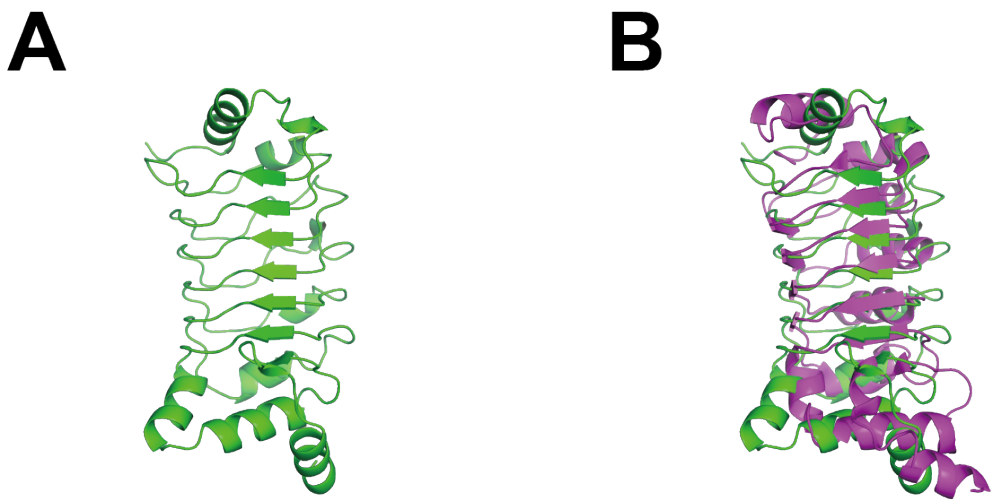


**Figure 2.5 Structural comparison of LC1 structures**

(A) Overall X-ray structure of LC1 (this study).

(B) Structural comparison of LC1 structures determined by X-ray (this study) and NMR (PDB ID: 1M9L). X-ray and NMR structures are colored green and magenta, respectively.

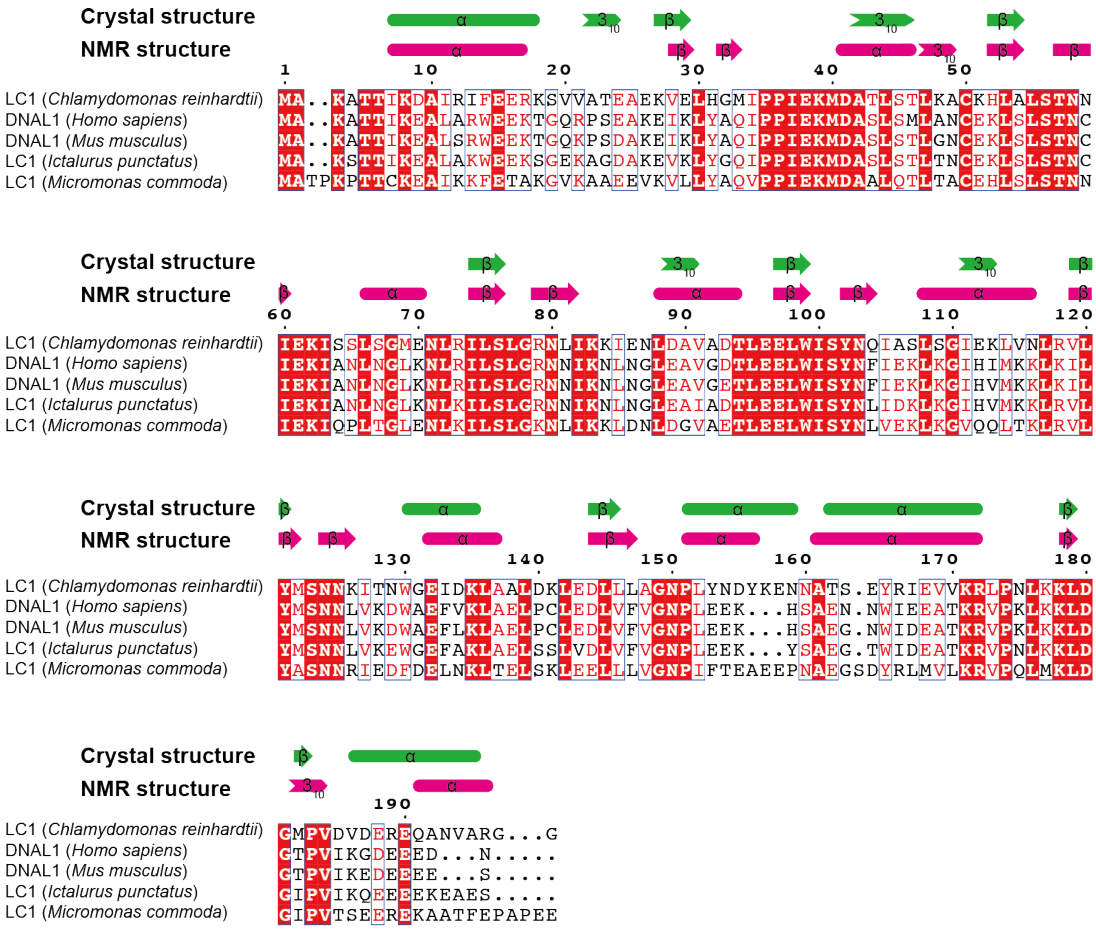


**Figure 2.6 Amino acid sequence alignment of LC1 with secondary structure assignments**

Secondary structure was calculated by STRIDE (49).

## Table 2.1. Crystallographic data and refinement statistics of LC1

| | |
|---|---|
| ***Data collection*** | |
| X-ray source | SPring-8 BL44XU |
| Wavelength (Å) | 0.90000 |
| Space group | $P2_12_12_1$ |
| Unit-cell parameters (Å) | $a$ = 53.54, b = 69.23, $c$ = 74.78 |
| Resolution (Å) | 50.00-1.55 (1.58-1.55) |
| Total reflection | 291518 |
| Unique reflections | 41149 (2043) |
| Completeness (%) | 99.8 (100.0) |
| $R_{merge}$ (%)[1] | 9.4 (94.6) |
| $\langle I/\sigma(I) \rangle$ | 36.5 (3.2) |
| ***Refinement*** | |
| Resolution (Å) | 36.85-1.55 |
| $R_{work}$[2]/$R_{free}$[3] (%) | 16.3/18.1 |
| Overall mean $B$-factor (Å$^2$) | 14.85 |
| Ramachandran plot (%)[4] | |
| Favored (%) | 96.1 |
| Allowed (%) | 3.9 |
| Disallowed (%) | 0.0 |
| r.m.s.d., bonds (Å) | 0.016 |
| r.m.s.d., angles (°) | 1.473 |

Values in parentheses are for the highest resolution shell.

[1] $R_{merge} = \sum_{hkl}\sum_i |I_i(hkl) - \langle I(hkl)\rangle| / \sum_{hkl}\sum_i I_i(hkl)$.

[2] $R_{work} = \sum_{hkl} \big||F_{obs}| - |F_{calc}|\big| / \sum_{hkl}|F_{obs}|$.

[3] $R_{free}$ is the R-factor computed for the test set of reflections that were omitted from the refinement process.

[4] Calculated by using MolProbity

### 2.3.2 Structural differences between X-ray and NMR structures

In particular, the structural differences in secondary structure between X-ray and NMR structures were remarkably large at Ala22-Glu24 and Met182-Val184 for N-terminal and C-terminal regions, respectively (Figure 2.7). The N-terminal region of X-ray structure formed a $3_{10}$ helix, but that of NMR structure formed a simple loop. On the other hand, the C-terminal region of X-ray structure formed a β-strand, but that of NMR structure was a $3_{10}$ helix instead. These structural differences suggest that these two regions may play a central role of flexible hinges and induces large conformational change starting at the both N- and C-terminal regions when LC binds to the target.

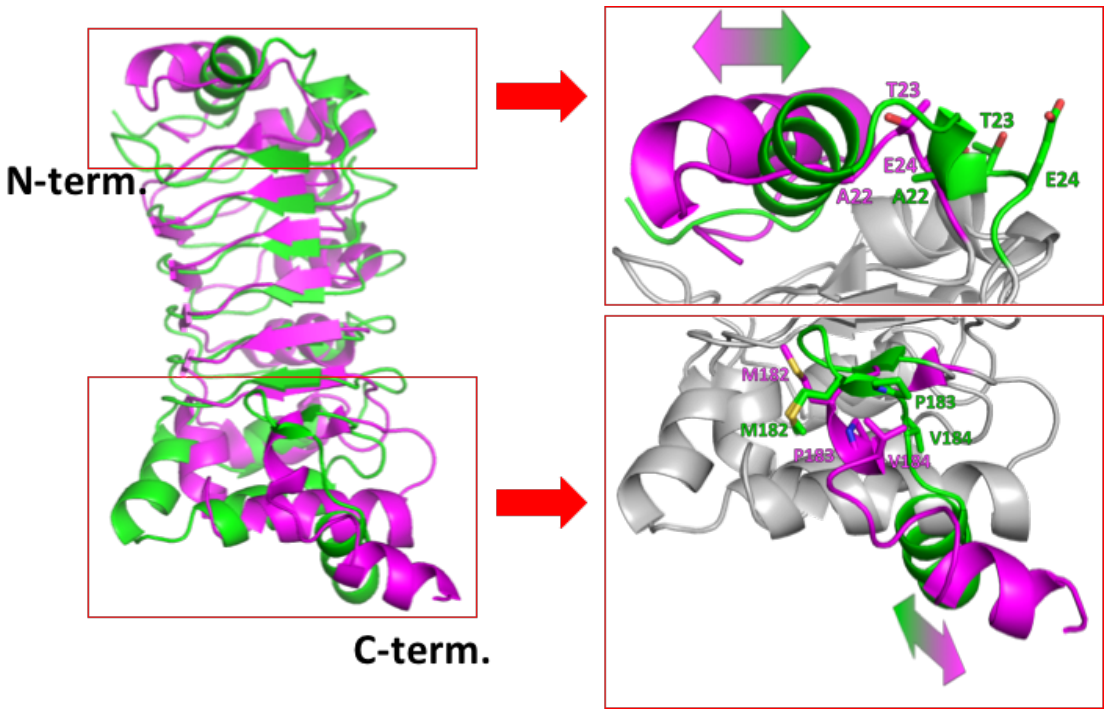


**Figure 2.7 Structural differences in N- and C-terminal regions**

X-ray and NMR structures are colored green and magenta, respectively.

### 2.3.3 Conformational flexibility of LC1

Next, I performed the TLS-refinement analysis after the final refinement cycle for LC1 in order to investigate the anisotropic conformational flexibility of LC1 in detail. In addition to structural comparison, I compared the resultant anisotropic B-factors of X-ray structure to the main-chain conformation of NMR structures, and found the local anisotropy in the X-ray structure (Figure 2.8). There were significant correlations between the directions of anisotropic B-factors of X-ray structure and the variety of main-chain conformations of NMR structure, which implies that the structural differences between X-ray and NMR structures are caused by intrinsic flexibility of LC1.

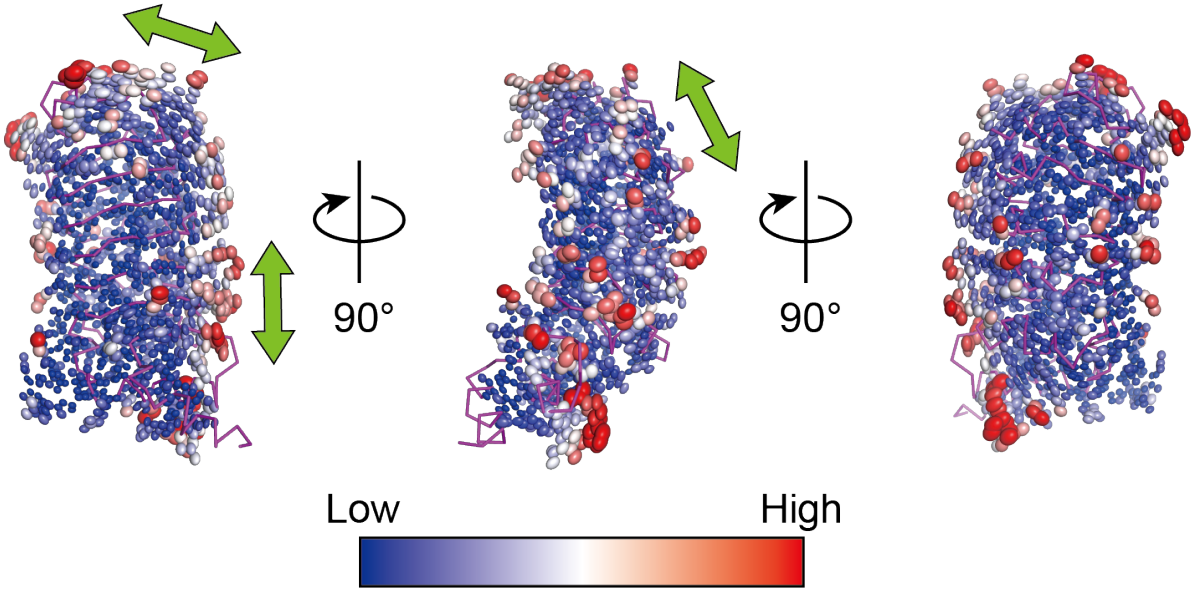


**Figure 2.8 Anisotropic B-factors of X-ray structure**

X-ray structure with anisotropic B-factors superposed on main-chain conformation of NMR structure (magenta).

## 2.4 Discussion

In this study, I determined the crystal structure of LC1 at 1.55 Å resolution. Furthermore, I revealed that the N- and C-terminal regions of LC1 are flexible enough to change their structures in secondary structure level and the conformational flexibility of LC1 is derived from its intrinsic property. In addition to the conformational flexibility of the N- and C-terminal regions, I found that the angle of the helix starting from Asn150 was clearly different between X-ray and NMR structures at the starting point of the helix. Being consistent with the structural insights, a mutation of Asn150, which is the terminal portion of LRR consensus sequence and located at the starting point of an α-helix, was reported to cause primary ciliary dyskinesia (PCD) (40). Moreover, a microtubule co-sedimentation assay had shown that negatively charged residues in the N-terminus region of LC1 is important for microtubule binding (35). Taken these data together, it is likely that the conformational changes in the N- and C-terminal regions of LC1 may contribute to the interaction with the OADγ HC or the microtubule. However, without the high resolution structural information of the real complex it is still unclear how LC1 binds to the partners, such as the OADγ. Thus I performed the structural analysis of the LC1-MTBD (OADγ) complex in Chapter 3.

# Chapter 3

# Structural analysis of LC1-MTBD complex

## 3.1 Introduction

Recently, it was discovered that LC1 binds to the MTBD of OADγ and is likely to regulate its motor activity as described in Chapter 1. The LC1 has been extensively characterized by mutational and structural analyses and the basic molecular mechanism of dynein HC including the MTBD has been investigated so far. However, it remains unclear how the LC1 interacts with the MTBD and regulates the function of OADγ. Thus, the purpose of this study is to bridge the gaps among independent studies of OADγ and LC1 by employing X-ray crystallography and mutational analysis of the LC1-MTBD (OADγ) complex.

## 3.2 Materials and Methods

### 3.2.1 Cloning

For expression of OADγ stalk region, the His-tagged stalk regions of the OADγ heavy chain gene from *Chlamydomonas reinhardtii* (UniProtKB: A8JFP1) were inserted into a modified pET17b plasmid. For expression as LC1-stalk complex, the GST-tagged LC1 gene (UniProtKB: Q9XHH2, 1-198 aa) from *Chlamydomonas reinhardtii* and the

His-tagged stalk regions of the OAD γ-heavy chain gene (UniProtKB: A8JFP1) from *Chlamydomonas reinhardtii* were inserted into a modified pET-17b plasmid with a sequence of ribosome binding site (agaaataattttgtttaactttaagaaggagatatacat) between the stop codon of LC1 and stalk for bi-cistronic expression (Figure 3.1). For the pull-down assay, stalk region (1542-1832aa) of the OADγ was used instead of the MTBD in the same construct, and the mutations were introduced by overlap extension PCR. To create α-registry fixed Stalk, stalk region (1598-1776 aa) of the OADγ was fused to a structurally stable artificial coiled-coil (AC) sequence to ensure the stable coiled coil packing (Figure 3.2) (50). And then it and GST-tagged LC1 gene were inserted into the modified pET17b in the same protocol of co-expression of LC1 and Stalk as described above. All constructs used in this study are summarized in Table 3.1.

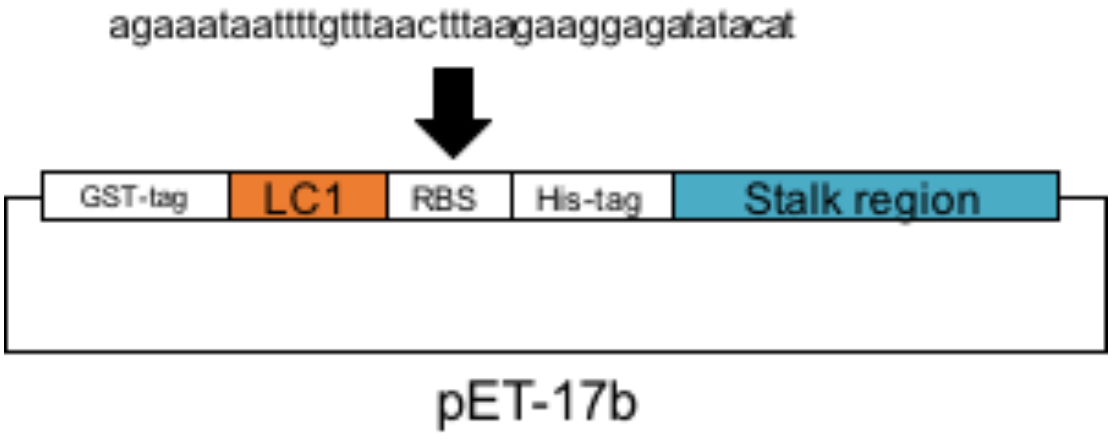


**Figure 3.1 Basic design of co-expression vector for LC1-Stalk complex**


**Figure 3.2 Construct design of α-registry fixed stalk (22:19) fused with a stable coiled coil**

The orange arrows show the positions of the conserved Pro residues. Sequences shown in red are AC, those shown in cyan are coiled coil of stalk.

**Table 3.1 Constructs for crystallization of LC1-Stalk complex**

| Construct | Stalk region |
|---|---|
| Stalk (79:75) | 1542-1832 |
| LC1-Stalk (79:75) | 1542-1832 |
| LC1-Stalk (40:32) | 1581-1789 |
| LC1-Stalk (22:14) | 1598-1771 |
| LC1-MTBD (7:0) | 1614-1757 |
| LC1-Stalk (α-registry fixed) (22:19) | 1598-1776 |

Length of the coiled coil of the stalk was shown as the numbers of residues from the conserved Pro located at CC1 and CC2.

### 3.2.2 Expression and purification

The plasmids were transformed into BL21(DE3) cells. Cells were pre-cultured at 37 ºC overnight, transferred to 1.5 L of modified LB medium (51) and cultured at 37 ºC overnight. The cells were harvested by centrifugation and stored at -80 ºC. Frozen cells

obtained from 4.5 L of culture were resuspended in 150 mL of buffer A (50 mM Tris-HCl (pH 8.0), 50 mM NaCl) supplemented with 1 mM benzamidine hydrochloride, 1 mM 6-aminocaproic acid, and 0.1 mM PMSF. The cells were lysed by sonication and the lysate was clarified by ultracentrifugation at 200,000g for 30 min. The supernatant was mixed with Ni-IMAC agarose (Bio-Rad) and then incubated at 4 ºC for 30 min. The agarose was washed with 5 column volumes of buffer B (50 mM Tris-HCl (pH 8.0), 50 mM NaCl, 10 mM Imidazole-HCl) and eluted by buffer C (50 mM Tris-HCl (pH 8.0), 50 mM NaCl, 300 mM Imidazole-HCl). The eluted sample was mixed with 1/70 (w/w) TEV protease to remove affinity tags and the buffer was exchanged to buffer D (10 mM Tris-HCl (pH 8.0), 50 mM NaCl) by dialysis at 20 ºC overnight. The sample was passed through Ni-IMAC agarose (Bio-Rad) and Glutathione sepharose 4B (Bio-Rad), and then loaded onto a HiLoad 16/600 Superdex 200 pg column (GE Healthcare) equilibrated in buffer D. Fractions containing the sample were pooled and concentrated. The sample was stored at -80 ºC until use. All other LC1-stalk constructs were purified in the same procedure.

### 3.2.3 Measurement of dynamic light scattering (DLS)

The Stalk (1542-1832 aa) sample was subjected to DLS measurement to quantify its homogeneity. Before the measurement, the sample was filtered by 0.2 μm filter (Merck). The measurement was performed using a DynaPro NanoStar instrument (Wyatt Technology) at 20 ºC. The sample was dissolved in buffer D. Data analysis was performed on Dynamics analysis software.

### 3.2.3 Crystallization and data collection

The LC1-Stalk (1542-1832 aa) crystals were grown at 4 ºC by the sitting drop vapor-diffusion method, in which 200 nL of Stalk (1542-1832 aa) (40 mg/mL in buffer D) was mixed with an equal volume of reservoir solution (0.1 M Tris-HCl pH 8.5, 2 M ammonium dihydrogen phosphate). The LC1–MTBD crystals were grown at 4 ºC by the sitting drop vapor-diffusion method, in which 200 nL of LC1–MTBD (70 mg/mL in buffer D) was mixed with an equal volume of reservoir solution (20 % PEG3350, 0.2 M sodium phosphate monobasic monohydrate). The crystals were soaked in a cryo-protectant solution (10 mM Tris-HCl (pH 8.0), 50 mM NaCl, 35 % PEG3350, 0.2 M sodium phosphate monobasic monohydrate) for several seconds, and then flash-cooled in liquid nitrogen. The X-ray diffraction experiment was performed at the beamline of BL44XU, SPring-8 (Harima, Japan).

### 3.2.4 Structure determination

The diffraction images of LC1-MTBD crystals were processed using HKL2000 software (44). The structure was solved by molecular replacement with Phaser-MR in the Phenix program suite (52) using the LC1 structure determined in the chapter 2 (PDB ID: 5YXM) as a starting model (53). Structural refinement was performed using phenix.refine in the Phenix program suite and COOT (54). The final structure was validated by MolProbity (48). The crystallographic data and refinement statistics are summarized in Table 3.2. The coordinates and structure factors for LC1–MTBD have been deposited in the worldwide Protein Data Bank under accession number 6L4P.

### 3.2.5 Pull-down assay

The transformed cells were cultured in 2 mL of modified LB medium at 37 ºC for overnight, and then harvested by centrifugation. Cells from 1 mL of culture were resuspended in 0.5 mL of buffer A and lysed by sonication. The lysate was clarified by centrifugation at 200,000g for 10 min. The supernatant was mixed with 10 μL of Ni-IMAC agarose (Bio-Rad) and then incubated at 4 ºC for 20 min. The agarose was washed three times with 400 μL of buffer A. Samples were eluted by adding 20 μL of buffer C. The eluted samples were mixed with 4 × SDS sample buffer and subjected to SDS-PAGE. Band intensities were measured by Quantity One software (Bio-Rad), and analyzed by SigmaPlot 13 (Systat Software, Inc).

## 3.3 Results

### 3.3.1 Crystallization of LC1-MTBD complex

In the beginning, I planned to prepare a crystallization sample by mixing separately purified LC1 and the stalk samples. When I purified a stalk region of OADγ (1542-1832 aa), it was eluted in the void volume during a gel-filtration chromatography (Figure 3.3). I pooled these fractions in the void volume, and subjected it to DLS measurement. As a result of the DLS measurement, the polydispersity of the stalk was 39.3% and the particle size analyzed by scattering curve was 20.73 nm (Figure 3.4). These results suggested that the stalk sample is aggregated as heterogeneous oligomer states.

Such a sample is not suitable for crystallization.

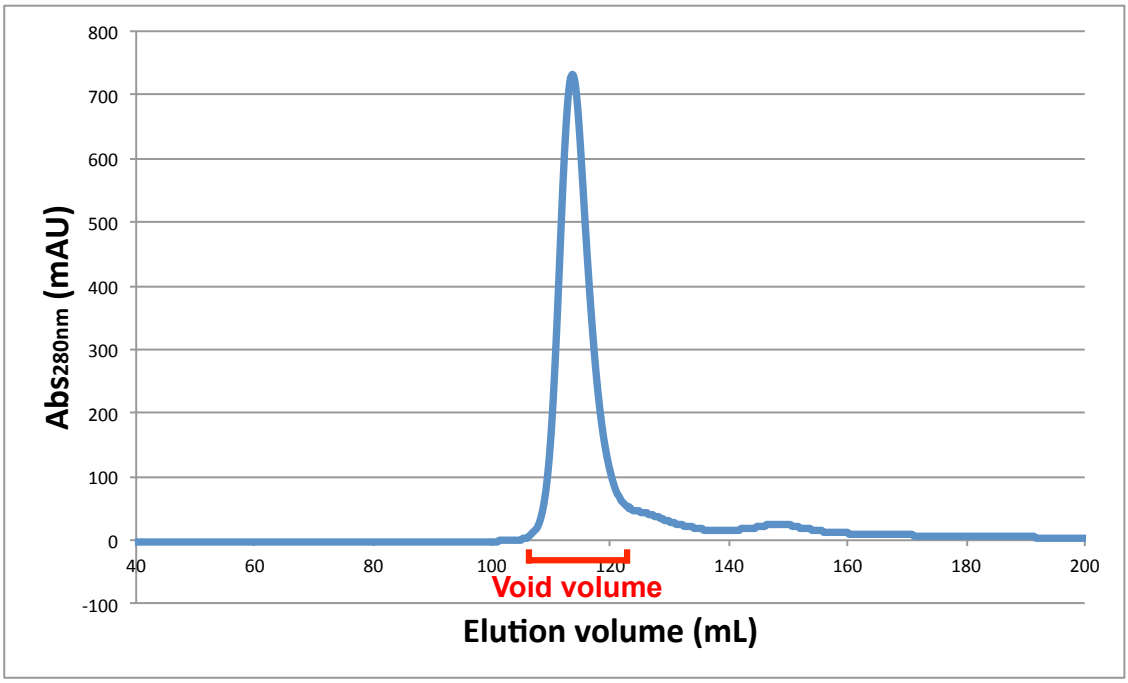


**Figure 3.3 Gel-filtration chromatography of the stalk (1542-1832 aa)**

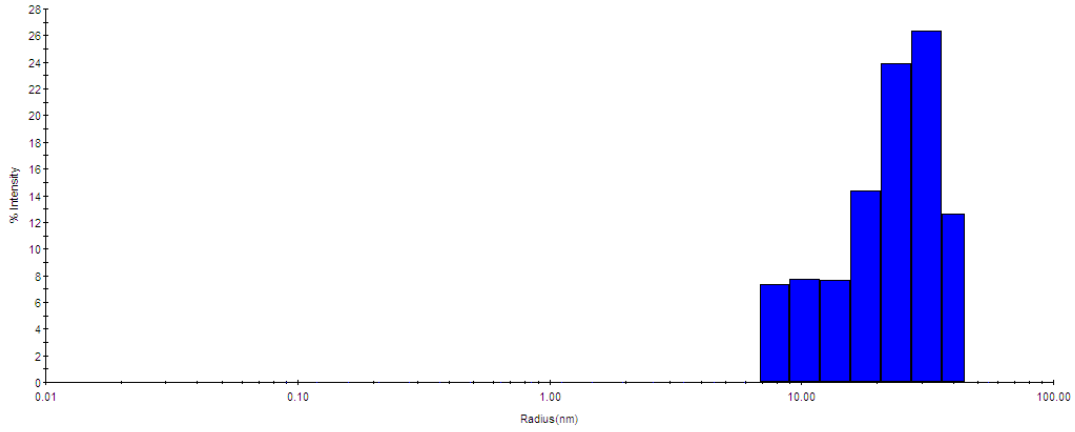


**Figure 3.4 Distribution of particle size of the Stalk (1542-1832 aa) analyzed by DLS**

Next, I tried to prepare a crystallization sample of LC1-Stalk by co-expression. I inserted the GST-tagged LC1 and the His-tagged stalk (1542-1832aa) genes into a modified pET17b plasmid with a sequence of ribosome binding site (RBS) between LC1 and the stalk genes for bi-cistronic expression. The sample can be purified successfully as a stable complex by the two-step purification using the Ni-affinity and gel-filtration chromatography (Figure 3.5). In gel-filtration, the sample was eluted in its proper elution volume compared with those of marker proteins. I performed crystallization screen of this purified sample for X-ray crystallography, and I obtained the crystals of LC1-stalk (1542-1832 aa) complex in a condition. However, the crystals of this complex were not suitable for X-ray data collection, because they were very thin and small (Figure 3.6). Although I tried to optimize the crystallization condition such as temperature, concentration of precipitant, and seeding method, the quality of the crystals did not be improved. Then, I created a series of deletion constructs that have different lengths of the coiled coil of stalk region for crystallization (Figure 3.7 and Table 3.1). I purified and crystallized these constructs as similar as the first trials, and I finally obtained good-looking crystals only of LC1-MTBD (1614-1757 aa) construct (Figure 3.8). Then, I collected the X-ray diffraction data from LC1-MTBD (1614-1757 aa) crystals and determined the structure (Figure 3.9 and Table 3.2).

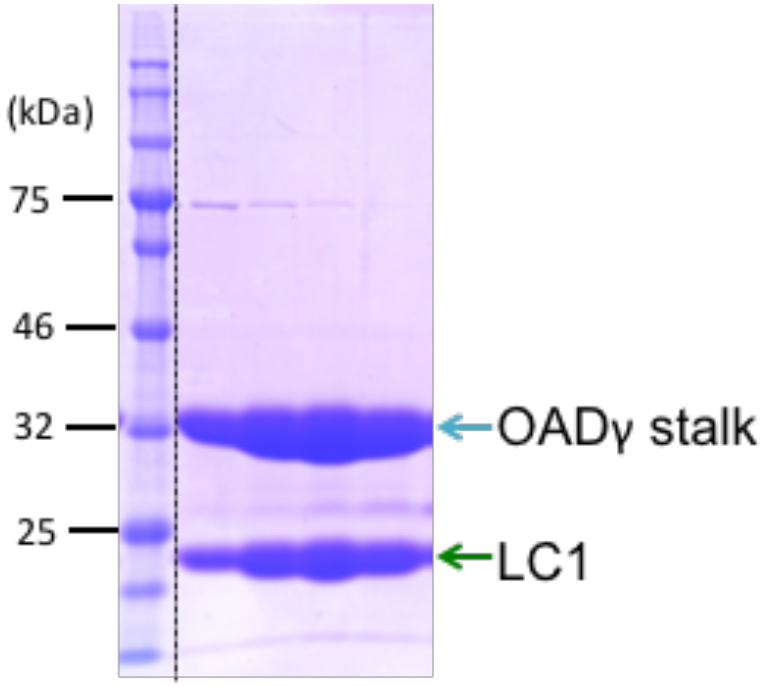


**Figure 3.5 SDS-PAGE of LC1-Stalk (1542-1832aa) complex**

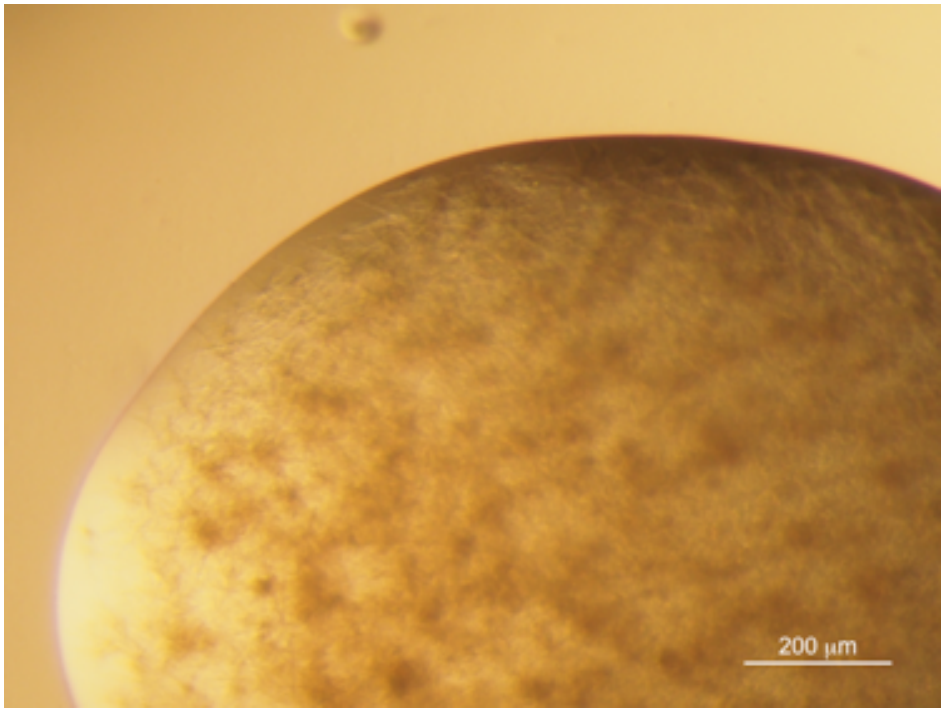


**Figure 3.6 LC1-Stalk crystals**

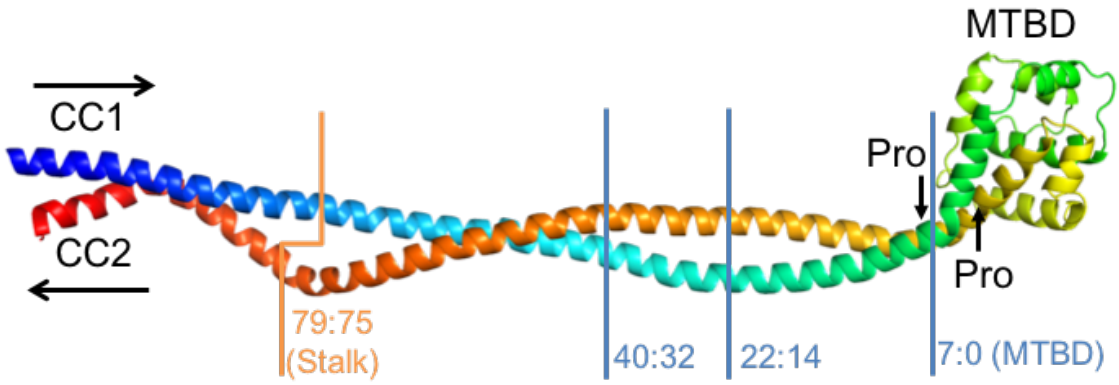


**Figure 3.7 Constructs of LC1-Stalk**

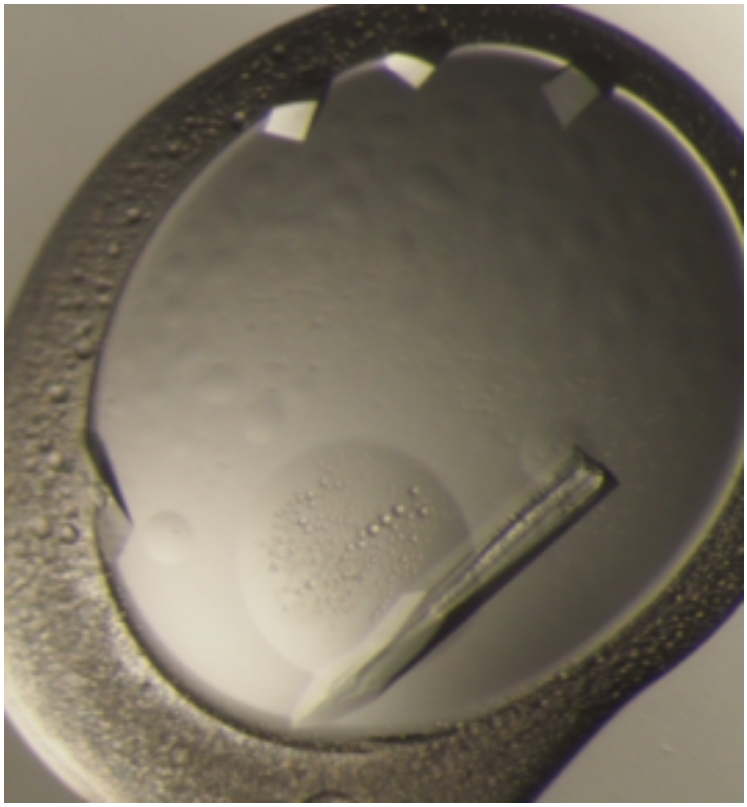

**Figure 3.8 LC1-MTBD crystals**

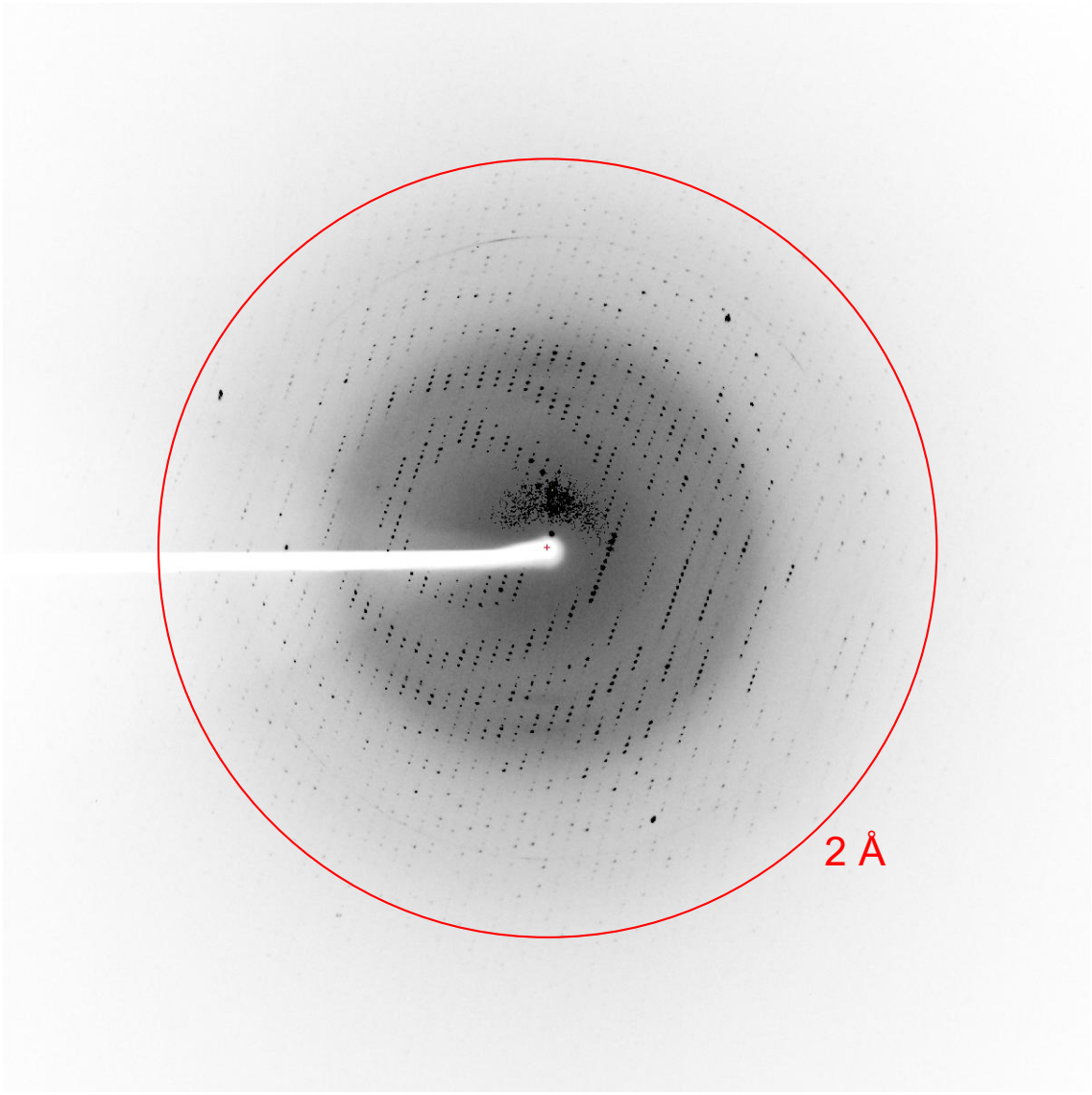


**Figure 3.9 X-ray diffraction image of the LC1-MTBD crystal**

### 3.3.2 Overall structure of the LC1-MTBD complex

I solved the crystal structure of the LC1–MTBD (1614-1757 aa) complex from *Chlamydomonas reinhardtii* at 1.7 Å resolution by X-ray crystallography (Fig. 3.10 and Table 3.2). The crystallographic asymmetric unit contained one molecule each of the LC1 and the MTBD, suggesting that LC1 is bound to the MTBD with a stoichiometric ratio of 1:1, as predicted previously (37). The MTBD interacted with the hydrophobic core of LC1 mainly *via* two regions, the H5 helix and the flap region (Figure 3.10).

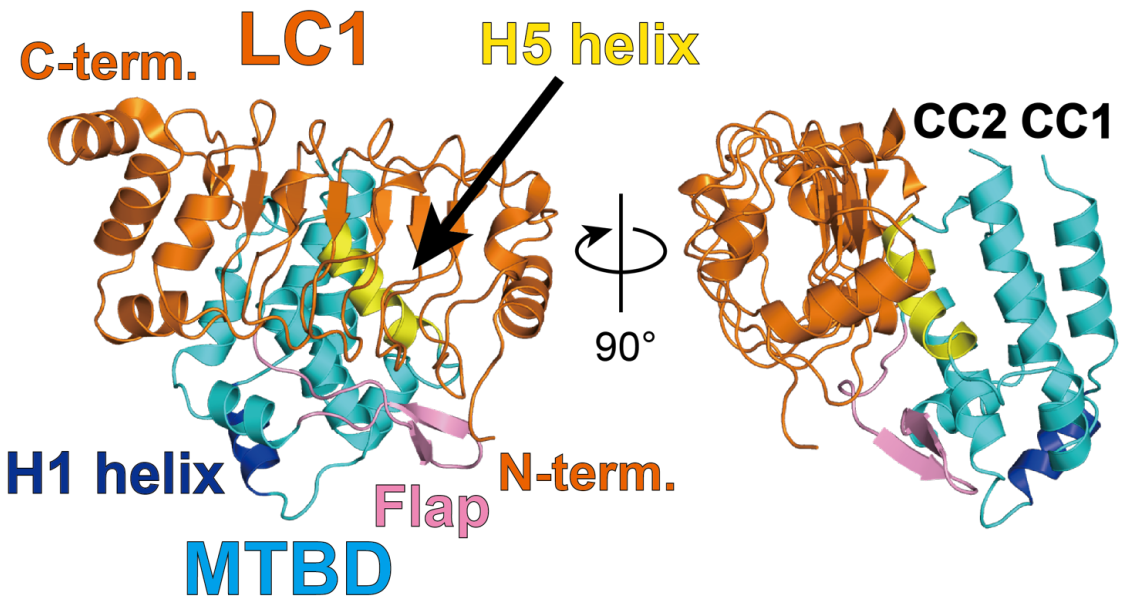


**Figure 3.10 Crystal structure of LC1–MTBD**

LC1 and the MTBD are colored in orange and cyan, and the H1 helix, the flap and the H5 helix of MTBD are shown in blue, pink, and yellow, respectively.

### 3.3.3 Structural comparison of LC1 structure

I compared the published NMR and X-ray structures (PDB ID: 1M9L and

5YXM) of LC1 alone (43, 53) to the newly obtained MTBD-complexed LC1 structure (Figure 3.11 A). The RMSD of Cα atoms between the new structure and the NMR or X-ray structure was 2.92 Å (134 aa) or 0.48 Å (194 aa), respectively, suggesting that the structure of LC1 in the MTBD complex is more similar to the X-ray structure than to the NMR structure. This is understandable because the X-ray structure is likely to mimic the complexed conformation due to overlap between interaction sites with the next crystallographic molecule and interaction sites with the MTBD (76.9 % residues of shared interaction sites), both of which shows low energy conformation of LC1 (Figure 3.12).

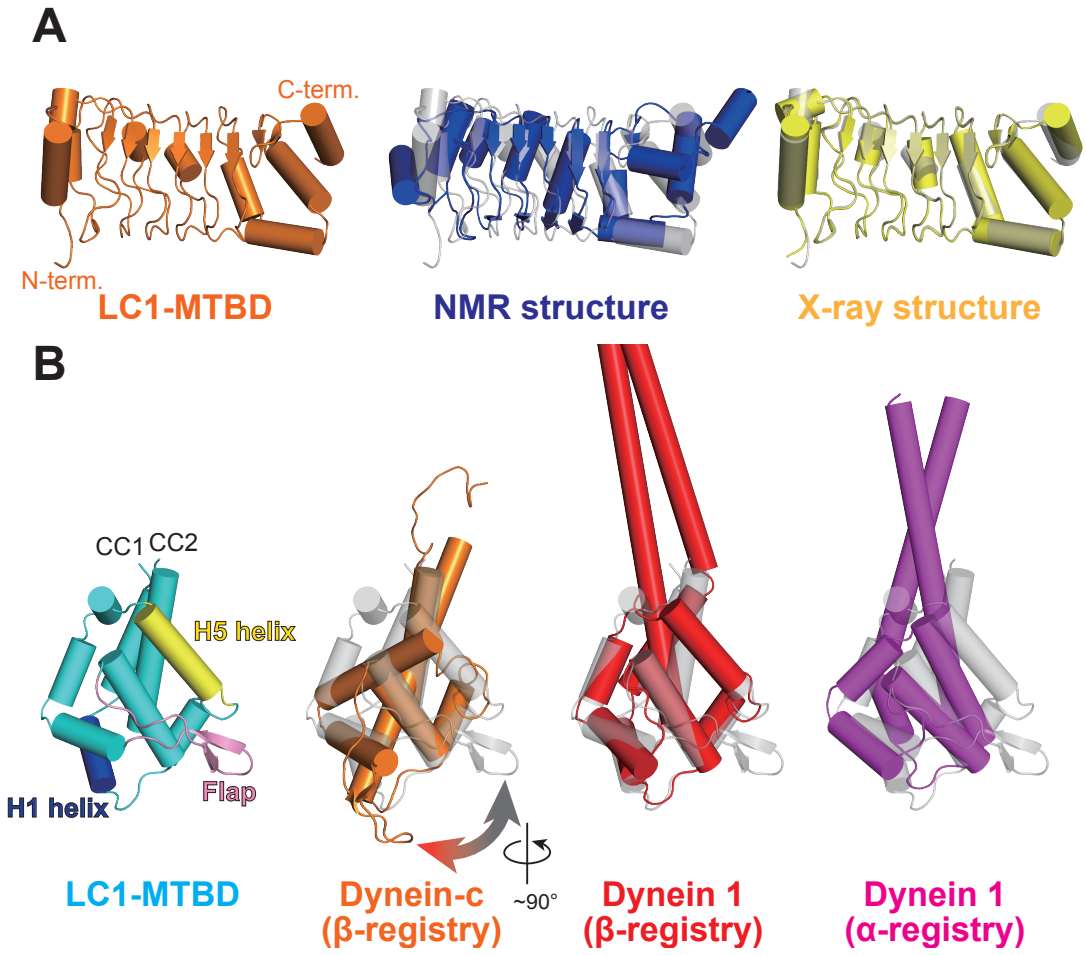


**Figure 3.11 Structural comparison of LC1 and MTBD in the LC1–**

**MTBD complex with known structures**

(A) Structural comparison of LC1. The LC1 structure in LC–MTBD, the NMR structure (PDB ID: 1M9L), and the X-ray structure (PDB ID: 5YXM) are shown in orange, blue, and yellow, respectively.

(B) Structural comparison of the MTBD. The MTBD structure in LC1–MTBD, that of dynein-c (PDB ID: 2RR7), that of dynein 1 in β-registry (PDB ID: 5AYH), and that of dynein 1 in α-registry (PDB ID: 3J1T) are shown in cyan, orange, red, and magenta, respectively.

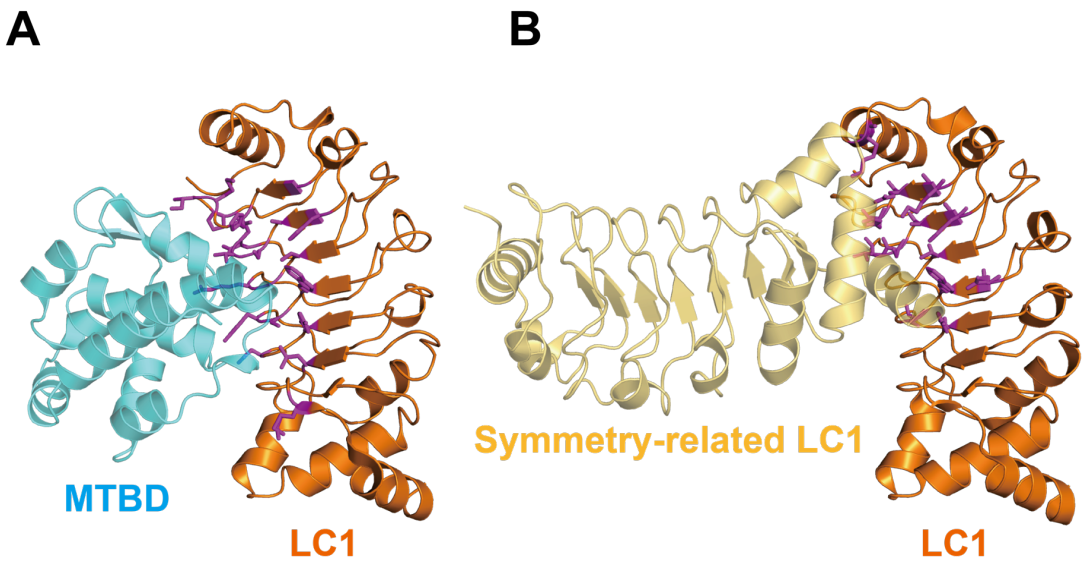


**Figure 3.12 Structural comparison of LC1**

(A) Crystal structure of LC1–MTBD.

(B) Crystal structure of LC1 and a symmetry-related molecule (X-1/2, -Y-1/2, -Z+1). Interaction residues are shown as stick models and colored magenta.

**Table 3.2 Crystallographic data and refinement statistics of LC1-MTBD**

| | |
|---|---|
| ***Data collection*** | |
| X-ray source | SPring-8 BL44XU |
| Wavelength (Å) | 0.9000 |
| Space group | $P2_12_12_1$ |
| Unit-cell parameters (Å) | $a$ = 44.55, b = 73.03, $c$ = 94.56 |
| Resolution (Å) | 50.00-1.70 (1.73-1.70) |
| Completeness (%) | 92.2 (89.4) |
| $R_{merge}$[1] (%) | 7.3 (76.6) |
| $\langle I/\sigma(I) \rangle$ | 31.7 (2.7) |
| ***Refinement*** | |
| Resolution (Å) | 39.69-1.70 |
| $R_{work}$[2]/$R_{free}$[3] (%) | 17.25/21.39 |
| Overall mean $B$-factor (Å$^2$) | 17.36 |
| Ramachandran plot (%)[4] | |
| Favored (%) | 97.57 |
| Allowed (%) | 2.43 |
| Outliers (%) | 0.0 |
| r.m.s.d., bonds (Å) | 0.006 |
| r.m.s.d., angles (°) | 0.794 |

Values in parentheses are for the highest resolution shell.

[1] $R_{merge} = \sum_{hkl}\sum_i|I_i(hkl) - \langle I(hkl)\rangle|/\sum_{hkl}\sum_i I_i(hkl)$.

[2] $R_{work} = \sum_{hkl}\big||F_{obs}| - |F_{calc}|\big|/\sum_{hkl}|F_{obs}|$.

[3] $R_{free}$ is the cross-validation R factor for the test set (5%) of reflections omitted from model refinement.

[4] Calculated by using MolProbity

### 3.3.4 Structural comparison of MTBD structure

I also compared the structure of the MTBD in the LC1–MTBD complex to structures of the MTBD from *Chlamydomonas* dynein-c (PDB ID: 2RR7), mouse cytoplasmic dynein 1 (PDB ID: 5AYH) and human cytoplasmic dynein 1 (PDB ID: 3J1T) (14, 18, 19) (Figure 3.11 B). Surprisingly, the conformations of the axonemal dynein-specific flap region differed significantly between the LC1-complexed MTBD and the single MTBD of dynein-c. In the LC1–MTBD structure, the flap was kinked approximately 90° around the axis parallel to the stalk as compared with that of dynein-c, indicating that the new conformation enables the flap to interact with LC1. I was also able to identify the structural state of the MTBD in terms of its affinity for microtubules, because the registry of the helical packing of stalk is exchangeable and linked to the microtubule-binding affinity. The RMSD of Cα atoms between the LC1-complexed MTBD and the MTBD of dynein-c or cytoplasmic dynein 1 (β-registry) was 2.13 Å (117 aa) or 1.74 Å (118 aa), respectively (11, 12). By contrast, between the complex and the MTBD of human cytoplasmic dynein 1 (α-registry) was 3.37 Å (111 aa) (21), suggesting that the LC1-complexed MTBD structure is in the β-registry, although the structure itself does not contain the coiled-coil region showing the actual registry of the helical packing.

The LC1 molecule alone possesses conformational flexibility as suggested by NMR, but it is clear from the complex structure that LC1 fixes the MTBD conformation to the β-registry if no structural or nucleotide-based restraints exist. This is compatible with the previous report that LC1 binding to the MTBD decreases the microtubule-binding affinity of the heavy chain (37).

### 3.3.5 Interactions between LC1 and MTBD

Next, I investigated the interaction between LC1 and the MTBD by pull-down assay. The MTBD binds to LC1 through the H5 helix and flap region with several hydrophobic and hydrophilic interactions (Figure 3.13 A, B, and Table 3.3). Complex formation involves a total of 41 residues (21 in LC1 and 20 in the MTBD) using a wide range of molecular surfaces. I selected 10 residues of LC1 for mutational analyses to assess the effect of electrostatic interaction (His31 and Arg79), hydrogen bonding (Ser56, Thr57, Asn59 and Tyr102) and hydrophobic interaction (Trp99, Tyr121, Met182 and Ile34). Mutational analysis showed that most of the mutations decreased binding activity slightly as compared with wild-type LC1 (Figure 3.13 C). Eight mutational sites (colored yellow and red in Figure 3.13 C) are involved in the interaction with the H5 helix and five with the flap (pink and red). These residues (Thr57, Arg79, and Tyr102), which are located in adjacent β-strand of the leucine-rich repeat in LC1, are the only residue that interacts with both the H5 helix and the flap (Fig. 3.14).

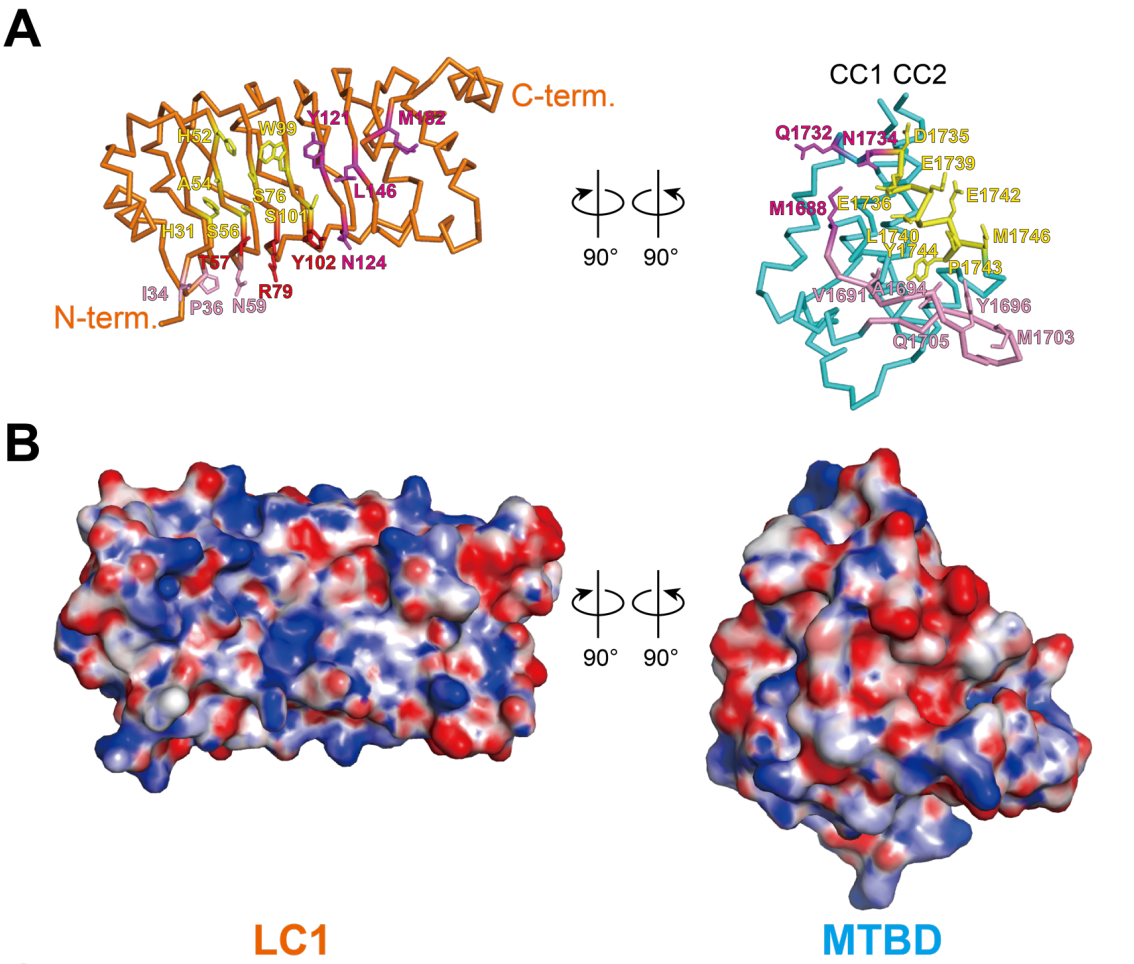


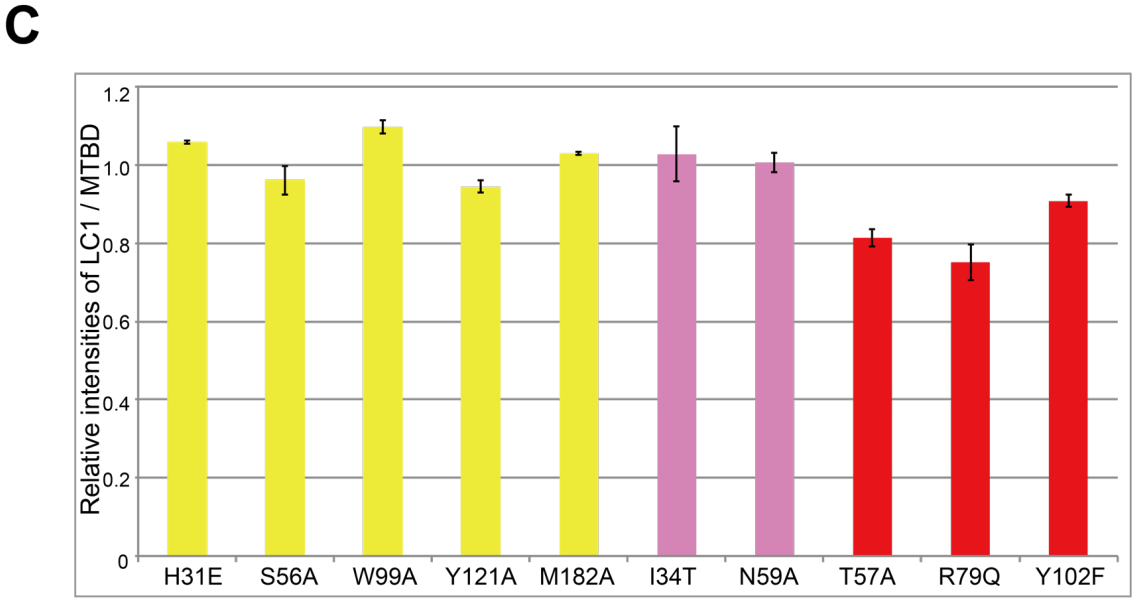


**Figure 3.13 Interactions between LC1 and the MTBD**

(A and B) Open book representation of the structure of LC1–MTBD. The interacting

residues with the H5 helix (yellow), the flap (pink), both in MTBD (red), and others (magenta) are shown as stick model in (A). The electrostatic potential of the surface is shown in (B).

(C) Pull-down assay of LC1 mutants. Residues that interact with the H5 helix, the flap, and both regions of the MTBD are shown in yellow, pink, and red, respectively. The values were normalized as the ratio of difference when the value of WT is 1, and averaged as the mean value ± SEM from three independent experiments.

## Table 3.3 Interactions between LC1 and the MTBD

| LC1 | MTBD | Hydrogen bonds | Non-bonded contacts |
|---|---|---|---|
| HIS 31 | GLU 1739 | - | 1 |
| HIS 31 | GLU 1742 | 1 | 2 |
| HIS 31 | MET 1746 | - | 3 |
| MET 33 | TYR 1696 | - | 1 |
| ILE 34 | TYR 1696 | - | 5 |
| ILE 34 | MET 1703 | - | 2 |
| PRO 36 | TYR 1696 | - | 1 |
| HIS 52 | GLU 1739 | 1 | 1 |
| ALA 54 | GLU 1739 | - | 3 |
| SER 56 | LEU 1740 | - | 1 |
| SER 56 | GLU 1739 | 1 | 3 |
| THR 57 | LEU 1740 | - | 1 |
| THR 57 | PRO 1743 | - | 2 |
| THR 57 | ALA 1694 | - | 1 |
| ASN 58 | ALA 1694 | - | 1 |
| ASN 59 | ALA 1694 | - | 3 |
| SER 76 | GLU 1739 | 1 | 2 |
| GLY 78 | GLU 1736 | - | 1 |
| ARG 79 | THR 1692 | 2 | 1 |
| ARG 79 | TYR 1744 | 2 | 3 |
| ARG 79 | VAL 1691 | - | 4 |
| ARG 79 | GLN 1705 | - | 1 |
| TRP 99 | GLU 1736 | - | 9 |
| TRP 99 | GLU 1739 | - | 1 |
| TRP 99 | ASP 1735 | - | 2 |
| SER 101 | GLU 1736 | 2 | 6 |
| TYR 102 | LEU 1740 | - | 1 |
| TYR 102 | VAL 1691 | - | 3 |
| TYR 102 | MET 1688 | - | 2 |
| TYR 102 | LEU 1689 | 1 | 3 |
| TYR 121 | GLU 1736 | - | 2 |
| TYR 121 | ASN 1734 | - | 8 |
| ASN 124 | MET 1688 | 1 | 2 |
| LEU 146 | MET 1688 | - | 2 |
| LEU 146 | ASN 1734 | - | 1 |
| GLY 181 | GLN 1732 | - | 3 |
| MET 182 | GLN 1732 | - | 3 |

Colored backgrounds correspond to the colors in Figure 3.13 C. The residues which interact at main chain are shown in brown. The number of hydrogen bonds and non-bonded contacts (hydrophobic interaction and other interactions) are summarized. These interactions were analyzed by LigPlot+ (55).

### 3.3.6 Interactions of the H5 helix and the flap

Among the mutational sites interacting with the H5 helix, T57A and R79Q mutations led to a substantial loss of activity (Figure 3.13 C). Thr57 is located close to Arg79 in an adjacent β-strand of the leucine-rich repeat in LC1 (Figure 3.14), implying that proper positioning of the adjacent Thr57 and Tyr102 residues around Arg79 places Arg79 in an optimal position for binding to both the H5 helix and the flap. The fact that these three residues, Thr57, Arg79 and Tyr102, are conserved from *Chlamydomonas reinhardtii* to *Homo sapiens* supports my interpretation.

Among the five mutational sites (Ile34, Thr57, Asn59, Arg79 and Tyr102) tested for interaction with the flap, only T57A and R79Q led to decreased binding while the other three showed similar binding affinity to that of wild-type LC1 (Figure 3.13 C), possibly because several other strong interactions remained (Figure 3.14).

I also compared the mean values of temperature factor of the flap and the H5 helix in order to investigate the flexibility of these regions. In the flap, the mean value of the temperature factor is almost same as all regions. In contrast, that in the H5 helix showed considerable low value, implying that the H5 helix is highly rigid (Table 3.4). Furthermore, the numbers of residues involved in the interaction between LC1 and the MTBD of the flap was eleven residues and that of the H5 helix was eighteen residues.

Overall, these results suggest that the contribution of the flap to the LC1–MTBD interaction is relatively minor relative to that of the H5 helix, although Arg79 is central to connecting the two types of interaction with the H5 helix and the flap.

Patel-King *et al*., has reported the phenotypic analysis of M182A mutant of

*Chlamydomonaus reinhardtii* (38). It is not surprising that mutation of M182 to Ala was least disruptive, because my mutational analysis in vitro showed almost no effect to the interaction between LC1(M182A) and MTBD as similarly as in vivo analysis.

**Table 3.4 Comparison of temperature factor ($Å^2$) in the flap and the H5 helix**

| | All regions | Flap | H5 helix |
|---|---|---|---|
| OADg | 22.50 | 22.31 | 15.61 |

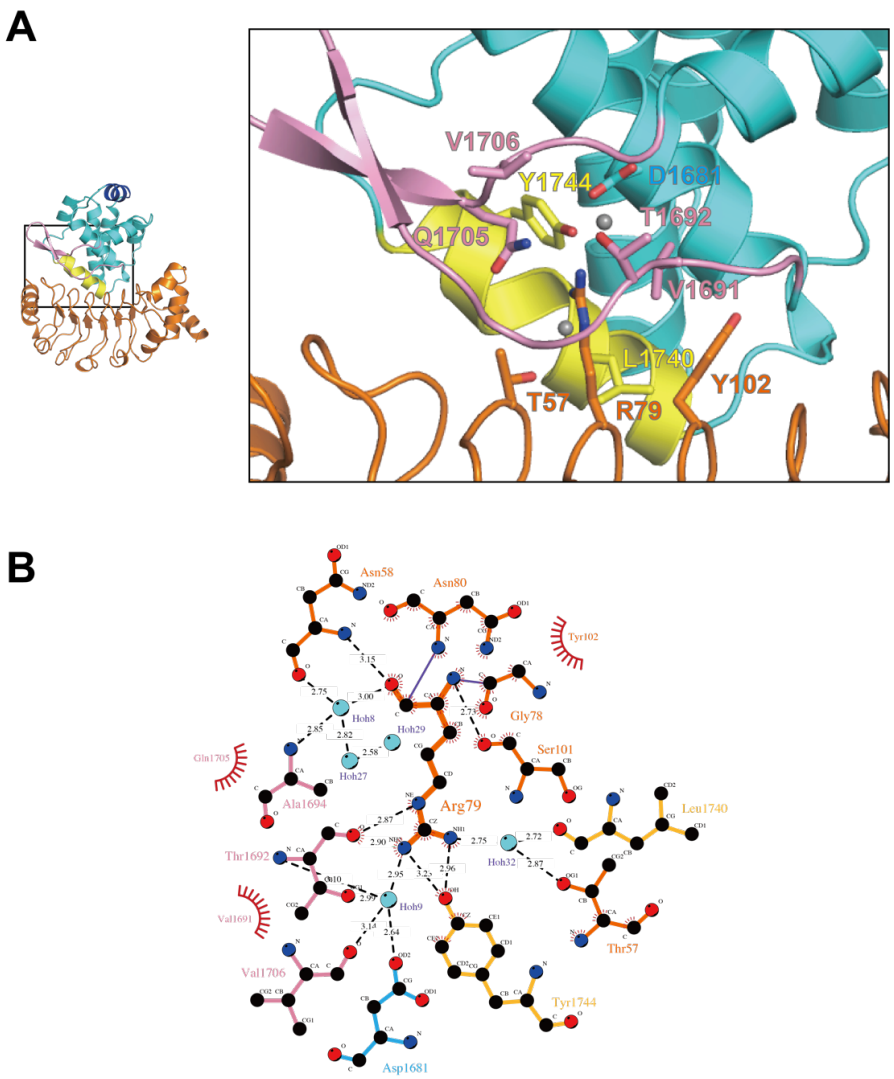


**Figure 3.14 Detailed view of the interactions between LC1 and the MTBD**

(A) Close-up of the interaction surface between LC1 and MTBD. LC1, MTBD, the flap, and the H5 helix are shown in orange, cyan, pink, and yellow, respectively. The residues that interact with Arg79 are shown as stick models.

(B) Detailed view of interactions with the flap region. The interactions were calculated by using LigPlot+ (55).

### 3.3.7 Modeled structure of microtubule-bound LC1-MTBD complex

Using a mid-resolution cryo-electron microscopy (cryo-EM) structure of the microtubule–cytoplasmic dynein MTBD complex (PDB ID: 3J1T) (19), I investigated how the LC1-complexed MTBD from OADγ (OADγ-MTBD) might bind to microtubules based on a hypothetically modeled structure of the ternary LC1–MTBD–microtubule complex. Using the MTBD core region of the OADγ-MTBD, the LC1–MTBD structure was superimposed onto the cryo-EM structure of the MTBD–microtubule complex (Figure 3.15) to predict the structure of the LC1–MTBD–microtubule complex.

In this modeled structure, the OADγ-MTBD was bound to α- and β-tubulins without any steric hindrance. Surprisingly, LC1 was located apart from the tubulins with no possibility of direct interaction with them. This is not consistent with the previous experimental results that the LC1 can bind dynein-depleted axonemes with low affinity, which seemed to result from the direct binding of LC1 to microtubules (35). It should be noted that none of the reported structures (including PDB ID: 3J1T) contain the flexible C-terminal tail (CTT) region of tubulin with the post-translational modification sites. Considering my structural model, it is possible that LC1 may bind to the invisible CTT regions of tubulins or to other accessory components contained in axonemes, which would position it near to the microtubules.

In the ternary model, the flap region of the OADγ-MTBD is positioned to connect LC1 and the MTBD, as mentioned above. Intriguingly, however, a recent cryo-EM study reported that the coulomb map of the axonemal dynein (DNAH7) MTBD bound on the microtubule shows an additional contact with the adjacent protofilament

(15). That study concluded that an extended flap region of the DNAH7-MTBD contacts the adjacent protofilament when the MTBD binds to the microtubule. Considering this new cryo-EM structure together with my modeled structure of the ternary LC1–MTBD–microtubule complex, it is possible that the folded flap region in my modeled structure may be released upon binding to the microtubule and interact with the adjacent protofilament, as suggested by the cryo-EM structure of the DNAH7-MTBD bound to microtubules.

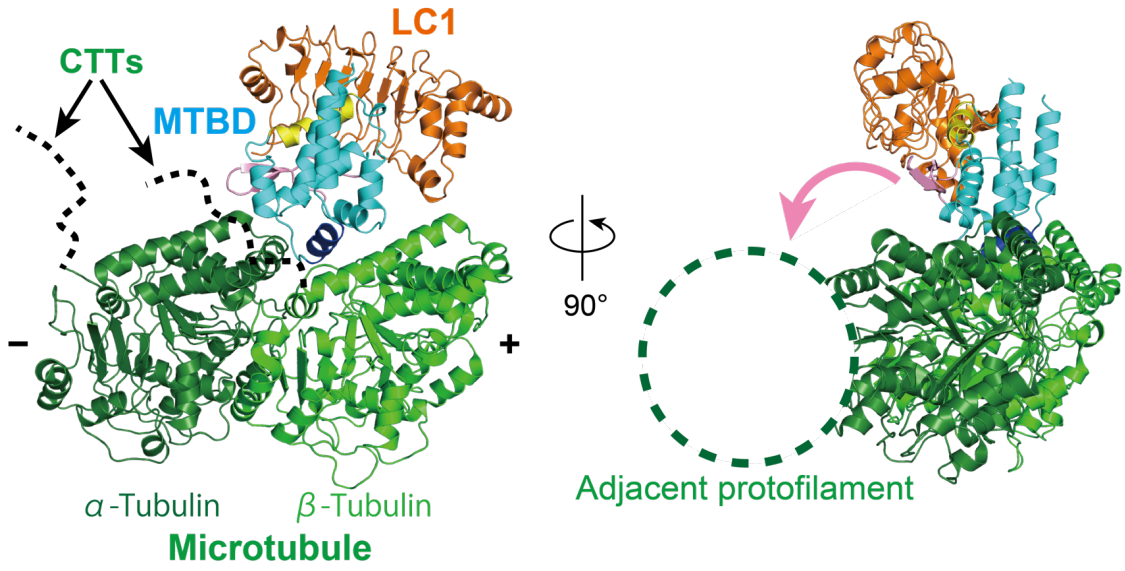


**Figure 3.15 Modelled structure of the microtubule-binding LC1–MTBD complex**

The crystal structure of LC1–MTBD was superimposed onto the cryo-EM structure of the MTBD–microtubule complex (PDB ID: 3J1T). Location of the C-terminal tails (CTTs) invisible due to their flexibility were shown as the dotted lines in the left panel. The pink arrow shown in the right panel explain the possible path for the flap to reach the

adjacent protofilament of microtubule.

## 3.4 Discussion

I revealed the complex structure of LC1 bound to the MTBD of OADγ by X-ray crystallography and identified two interaction sites of MTBD for LC1, the H5 helix and the flap region. In addition to the structural analysis, I performed a structure-based mutational analysis using a pull-down assay and ten LC1 mutants to evaluate the importance of these two sites. The interaction surface and points between LC1 and the MTBD are so wide (buried surface area: 1021.1 $Å^2$) and intense (Figure 3.13 A) that the effects of a single mutation were not marked; however, mutation of Arg79 in LC1, which is positioned between the H5 and flap interaction sites of the MTBD (Figure 3.14 A), weakened the interaction between the two proteins. I assume that Arg79 may help in coordinating interactions by the H5 helix and the flap in the MTBD. In fact, Arg79 and its surrounding residues, such as Thr57 and Tyr102, are well conserved from *Chlamydomonas reinhardtii* to *Homo sapiens* as mentioned above. The residues of MTBD interacting with LC1 were not entirely conserved in the other axonemal MTBDs (Figure 3.16). This result might be a reason why LC1 binds only to OADγ.

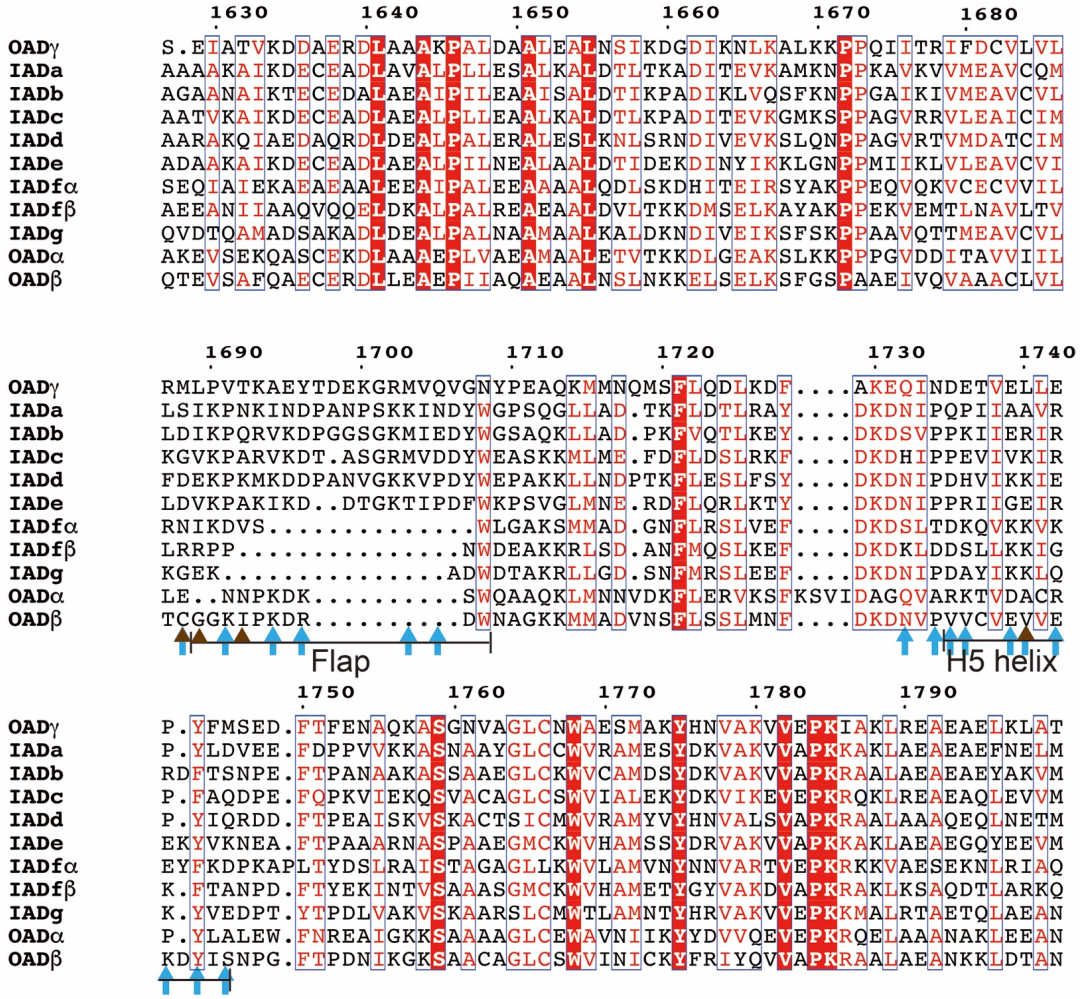


**Figure 3.16 Amino acid sequence alignment of axonemal dynein MTBDs from *Chlamydomonas reinhardtii***

Amino acid sequences of OADγ (UniProtKB: A8JFP1), IADa (UniProtKB: A8I5C3), IADb (UniProtKB: A8I3X6), IADc (UniProtKB: Q4AC22), IADd (UniProtKB: A8J063), IADe (UniProtKB: A8ISA6), IADfα (UniProtKB: Q9SMH3), IADfβ (UniProtKB: Q9MBF8), IADg (UniProtKB: A8IV22), OADα (UniProtKB: A8J336), and OADβ (UniProtKB: A8J1M5) were aligned. The residues which interact with LC1 by its side chain and those that interact through the backbone are shown in cyan arrows and brown arrowheads, respectively. These interactions were analyzed by LigPlot+ (55).

This study indicates that LC1 is not able to bind directly to the microtubule track in its current binding geometry. Here it should be noted that LC1 is also able to interact with the MTBD stably even in α-registry. When I screened suitable constructs for crystallization, I prepared several variants with different coiled-coil lengths, and one of which fixed the α- or β-registry by the stable artificial coiled coil at the base. The construct artificially fixed in the α-registry was designed as similarly as the case of previous cryo-EM analysis (56); My preliminary results showed that LC1 could also bind to MTBD molecules that had been artificially fixed in the α-registry (Figure 3.17); this is not surprising because my documented interactions in this study between LC1 and the MTBD were broad and intense, as pointed out above. How, then, can LC1 alter the MTBD binding affinity and ultimately tune cilia/flagella activity? The clear structural difference in the MTBD flap region between my complex structure and the dynein-c structure (Figure 3.11 B) may be central to discussions of the basis for the regulatory function of LC1.

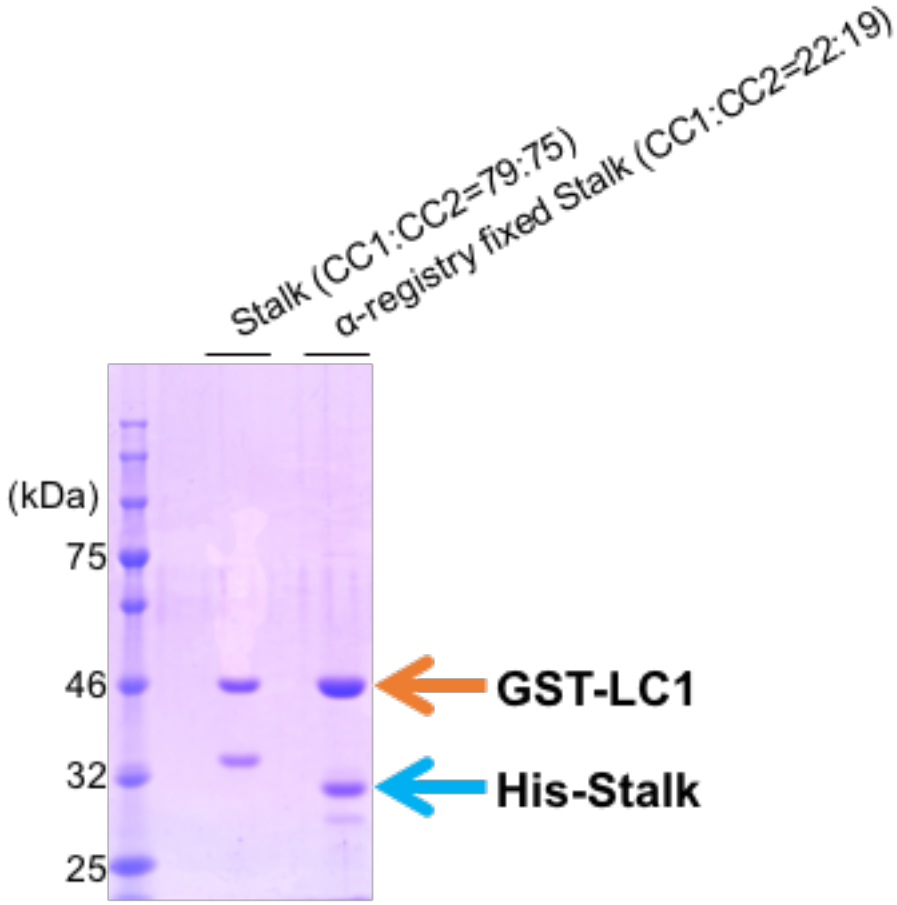


**Figure 3.17 Purification of LC1-Stalk (α-registry fixed) complex**

To examine how much the interactions between LC1 and the flap region observed in this study are conserved, the amino acid sequences of various MTBDs of OADγ were aligned and analyzed (Figure 3.18). I found that the interaction sites in the flap region of OADγ are not conserved except for Asp1681 near the root of the flap (Figure 3.14 A), suggesting that the interaction of LC1 with the H5 helix is physiologically dominant, while that with the flap region is relatively minor. This hypothesis is consistent with the ratio of residues involved in the two sites of interaction

between LC1 and MTBD (20 residues for the H5 helix, and 14 residues for the flap region). These results may suggest that the interactions between the flap and LC1 are specific but also relatively weak and easily cancelled, consequently tethering or releasing the flap to/from the MTBD. These two structural states of the flap may be a key to discuss about the physiological functions of LC1. In addition, a recent cryo-EM study showed that the extended flap of the DNAH7-MTBD contacts the adjacent protofilament (15). Thus, in certain condition, the flap released from the MTBD might be able to bind to the adjacent protofilament in the same manner of DNAH7 (Figure 3.15).

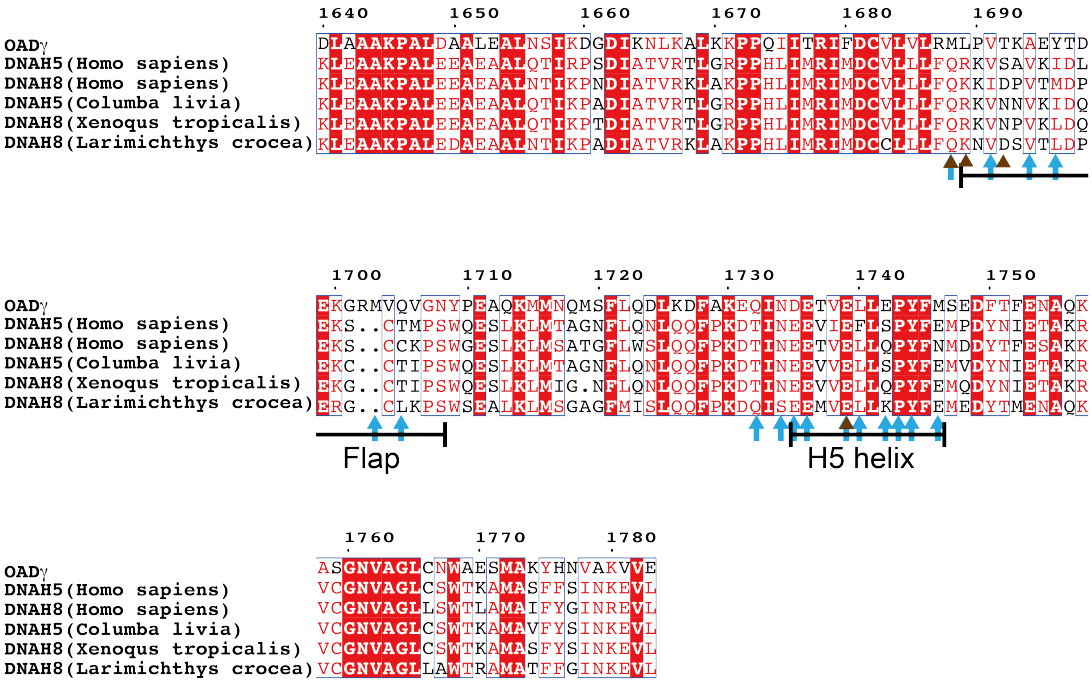


**Figure 3.18 Amino acid sequence alignment of MTBDs of OADγ**

Amino acid sequences of OADγ from *Chlamydomonas reinhardtii* (UniProtKB: A8JFP1), DNAH5 from *Homo sapiens* (UniProtKB: Q8TE73), DNAH8 from *Homo sapiens* (UniProtKB: Q96JB1), DNAH5 from *Columba livia* (RefSeq: XP_021143896.1),

DNAH5 from *Xenopus tropicalis* (RefSeq: XP_012820905.1), and DNAH8 from *Larimichthys crocea* (RefSeq: XP_019109781.2) were aligned. The residues which interact with LC1 by its side chain and those that interact through the backbone are shown in cyan arrows and brown arrowheads, respectively. These interactions were analyzed by LigPlot+ (55).

This is a summary of newly obtained and already published information together. (I) LC1 is not directly bound to the microtubule with enough space left between the microtubule track and LC1, and may interact remotely with the CTTs of tubulins. (II) The binding of LC1 to MTBD is so tight that LC1 would bind to the MTBD permanently through the main interaction with the H5 helix, (III) but the extended flap region of DNAH7 (human axonemal dynein which does not bind to LC1) can bind to the adjacent protofilament and strengthen the interaction with the microtubule. (IV) LC1 can alter the binding affinity of MTBD to the microtubule weaker and (V) ultimately tune cilia/flagella activity. Based on these five pieces of information collectively, I propose a new structural mechanism in which LC1 may act as a regulatory switch that tethers or releases the flap to/from the MTBD in accordance with the local curvature of the microtubule for appropriate stepping of OADγ (Figure 3.19). The regulatory stepping mechanism of the OADγ-MTBD would proceed as follows. (i) When the OADγ-MTBD is not bound to the microtubule, LC1 tethers the flap region as observed in the current X-ray structure. (ii) When the OADγ-MTBD binds to the microtubule in a nucleotide-dependent manner, LC1

is still tethering the flap from the MTBD to prevent it from reaching to the microtubule and making the interaction stronger. (iii) If the microtubule becomes closer to the flap tethered by LC1 depending on its local curvature (upper right panel of Figure 3.10), the flap is released probably because of much stronger interaction against the adjacent protofilament of microtubule. (iv) After the power stroke accompanying the ATPase cycle in the AAA+ ring domain, the OADγ-MTBD detaches from the microtubule track and returns to the state in (i). In this model, LC1 is able to prevent the flap being involved in the additional interaction with the microtubule depend on its local curvature and eventually weaken the relative affinity to the microtubule compared to the case in absence of LC1.

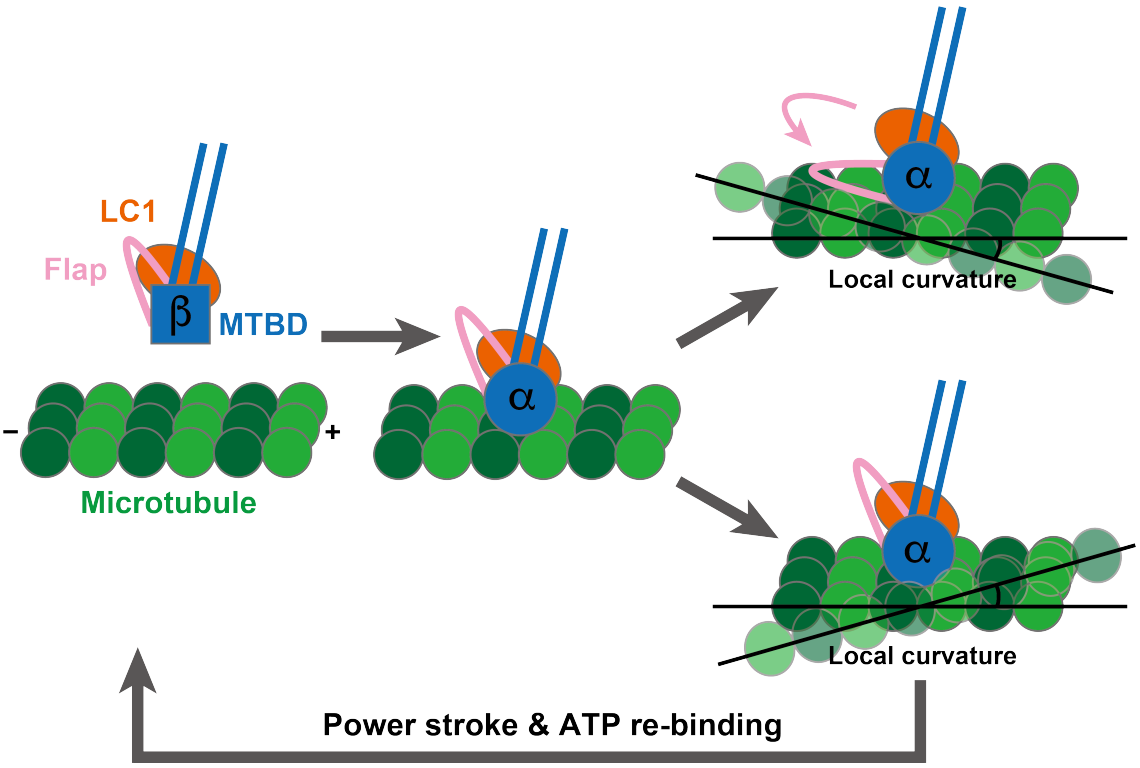


**Figure 3.19 Proposed model of curvature sensing by LC1**

My model may be partly supported by a previous *in vitro* 3D motility assay of microtubule sliding driven by OADα of *Tetrahymena* (OADα, β and γ from *Tetrahymena* correspond to OADγ, β and α from *Chlamydomonas*) (27). All OADs of *Tetrahymena* caused a clockwise rotation of each sliding microtubule around its longitudinal axis but only OADα (corresponding to *Chlamydomonas* OADγ) can tune the clockwise screwing pitch, whereas the OADβγ complex did not display any sensitivity. LC1 would be a regulatory protein to switch the additional microtubule binding site of OADγ on or off, resulting in a rotational sliding of microtubule in gliding assay. To confirm our proposed mechanistic model of curvature sensing *in vivo*, the further functional studies using *Chlamydomonas* mutant cells are needed and already on-going.

# Chapter 4

# X-ray crystallographic analysis of IAD (DNAH10) MTBD

## 4.1 Introduction

In chapter 3, I determined the crystal structure of LC1-MTBD, and provided a novel insight into molecular roles of the OADγ in flagellar beating. However, there are many axonemal dynein heavy chains (at least 15 HC genes present in most eukaryote) most of which are structurally unknown, and these dynein heavy chains display distinct motor properties. To understand how a microtubule sliding generated by an individual axonemal dynein is coordinated to form a bending as a whole axoneme, more precise mechanistic/structural information on axonemal dyneins are needed.

In this chapter, I focus on structural and functional differences of axonemal dynein MTBD in stalk region. The amino acid sequence analysis showed that the number of amino acids comprising a stalk region is highly conserved in various organism but there are several insertions in MTBD (Figure 3.9). The most remarkable difference is a flap, which is about 11-16 aa insertion observed in several axonemal dyneins (IADa, b, c, d, e, and OADγ in *Chlamydomonas*) and forms a β-hairpin structure (14). These characteristic insertions and differences of the sequences would contribute to the distinct motor function. In contrast, an unique study of synthetic biology had demonstrated that

hybrid dyneins with actin binding proteins instead of the MTBD could slide actin filaments to the opposite direction (57), implying that MTBD itself is not responsible for determination of the moving direction. But the gliding velocity of these hybrid motors decreased by two orders of magnitude compared to the wild type, suggesting that the MTBD is not mandatory but necessary for the precise motor function. Therefore, in this Chapter, I describe the structural study of diversity of MTBDs toward comprehensive understanding of molecular mechanism based on the X-ray crystallographic study of IAD (DNAH10) MTBD.

## 4.2 Materials and Methods

### 4.2.1 Construct

The His-tagged MTBDs (CC1:CC2 = 7:0) of DNAH1 (UniProtKB: Q9P2D7, 2912-3054 aa), DNAH2 (UniProtKB: Q9P225, 3087-3214 aa), DNAH7 (UniProtKB: Q8WXX0, 2668-2811 aa), DNAH9 (UniProtKB: Q9NYC9, 3149-3283 aa), and DNAH10 (UniProtKB: Q8IVF4, 3127-3255 aa) from *Homo sapiens* were inserted into a modified pET17b plasmid. The cDNAs of DNAH1, DNAH2, DNAH7, DNAH9, and DNAH10 were purchased from Kazusa DNA Research Institute.

### 4.2.1 Expression check

The plasmids were transformed into BL21(DE3) cells. The cells were cultured at 37 ºC for 7 hours and then continued to culture at 20 ºC overnight in 2 mL of the

modified LB medium (51). The cells were harvested and suspended in buffer A (50 mM Tris-HCl (pH 8.0), 100 mM NaCl) and lysed by sonication. The lysed samples were centrifuged at 15000 g for 10 mins to separate soluble and insoluble fractions. Expression of the target proteins were judged by SDS-PAGE.

### 4.2.2 Expression and purification

The plasmids were transformed into BL21(DE3) cells. The cells were pre-cultured at 37 ºC overnight, transferred to 1.5 L of modified LB medium supplemented with 100 μg/mL and cultured at 20 ºC overnight. The cells were harvested and stored at -80 ºC. The frozen cells were suspended in buffer A (50 mM Tris-HCl (pH 8.0), 100 mM NaCl) supplemented with 1 mM benzamidine hydrochloride, 1 mM 6-aminocaproic acid, and 0.1 mM PMSF. The cells were lysed by sonication and the lysate was centrifuged at 200,000g for 20 min. The supernatant was mixed with Ni-IMAC agarose (Bio-Rad) and incubated at 4 ºC for 20 min. Then, the agarose was washed with buffer B (buffer A + 10 mM Imidazole-HCl) and eluted by buffer C (buffer A + 300 mM Imidazole-HCl). The sample was mixed with 1/70 (w/w) TEV protease to remove the His tag and the buffer was exchanged to buffer D (10 mM Tris-HCl (pH 8.0), 100 mM NaCl) by dialysis at 4 ºC overnight. The sample was passed through Ni-IMAC agarose (Bio-Rad) then subjected to a HiLoad 16/600 Superdex 200 pg column (GE Healthcare) equilibrated in buffer D. Fractions containing DNAH10 MTBD were pooled and concentrated to 15 mg/mL. The sample was stored at -80 ºC until use. For single wavelength anomalous dispersion (SAD) experiment, I used B834 (DE3) pLysS cells instead of BL21 (DE3) and then cultured

using LeMaster medium supplemented with 5μg/mL of Vitamin B1 and 25 μg/mL of L-selenomethionine (SeMet). The SeMet substituted sample was purified in the same protocol.

### 4.2.3 Crystallization and data collection

DNAH10 MTBD crystals were grown at 4 ºC by the hanging drop vapor-diffusion method, in which 1 μL of DNAH10 MTBD was mixed with an equal volume of reservoir solution (25 % PEGMME 550, 0.1 M Trisodium citrate (pH 4.9), 10 mM Praseodymium (III) acetate). The crystals containing the SeMet substituted sample were grown at 4 ºC by the hanging drop vapor-diffusion method, in which 1.5 μL of the sample was mixed with 1 μL of reservoir solution (25 % PEGMME 550, 0.1 M Tri-sodium citrate (pH 4.9), 10 mM Praseodymium (III) acetate) and 0.5 μL of seed solution (25 % PEGMME 550, 0.1 M Trisodium citrate (pH 4.9), 10 mM Praseodymium (III) acetate, 10 mM Tris-HCl (pH 8.0), 100 mM NaCl). The crystals were soaked in a cryo-protectant solution (35 % PEGMME 550, 0.1 M Tri-sodium citrate (pH 4.9), 10 mM Praseodymium (III) acetate, 10 mM Tris-HCl (pH 8.0), 100 mM NaCl) for several seconds, and then flash-cooled in liquid nitrogen. The X-ray diffraction experiment was performed at the beamline of BL44XU, SPring-8 (Harima, Japan).

### 4.2.4 Structure determination

The diffraction images were processed using XDS program (58). A crystallographic phase problem was solved by SAD method using Phenix AutoSol in

phenix program suite (59). Structure refinement was performed using phenix.refine in phenix program suite (52, 60) and COOT software. The final structure was validated using the wwPDB validation server. The crystallographic data and refinement statistics are summarized in Table 4.1.

## 4.3 Results

### 4.3.1 Structure determination of DNAH10 MTBD

In the beginning, I tried to express and purify various MTBDs from *Homo sapiens* (DNAH1 (IADd), 2 (IADfβ), 7 (IADa), 9 (OADβ), and 10 (IADfα)) to investigate whether there is any structural and functional difference between them. As a result of expression check, all constructs were highly expressed in *E.coli*. However, the MTBDs of DNAH1, DNAH7, and DNAH9 were mainly isolated in insoluble fraction (Figure 4.1). By contrast, the MTBDs of DNAH2 and DNAH10 were isolated in soluble and insoluble fractions at ratio of 1:1 (Figure 4.1). Among all constructs, I could purify two MTBDs (DNAH2 and 10) and then obtain crystals only from DNAH10 MTBD (Figure 4.2). I performed X-ray diffraction experiment using DNAH10 MTBD crystals (Figure 4.3) and tried to determine the structure. However, I couldn't get good initial phase angles by molecular replacement (MR) method, then I carried out the SAD experiment using SeMet substituted sample. I could successfully prepare the SeMet substituted sample as same as the native one, and collected diffraction data for SAD at 1.8 Å resolution. The SAD calculation has confirmed that a asymmetric unit contains four MTBD molecules. The

Matthews coefficient ($V_M$) of the crystal was estimated to be 2.16 $Å^3Da^{-1}$ and its solvent content was 43.06 % (61). Finally, I determined the crystal structure of DNAH10 MTBD at 1.5 Å resolution (Figure 4.4 and Table 4.1).

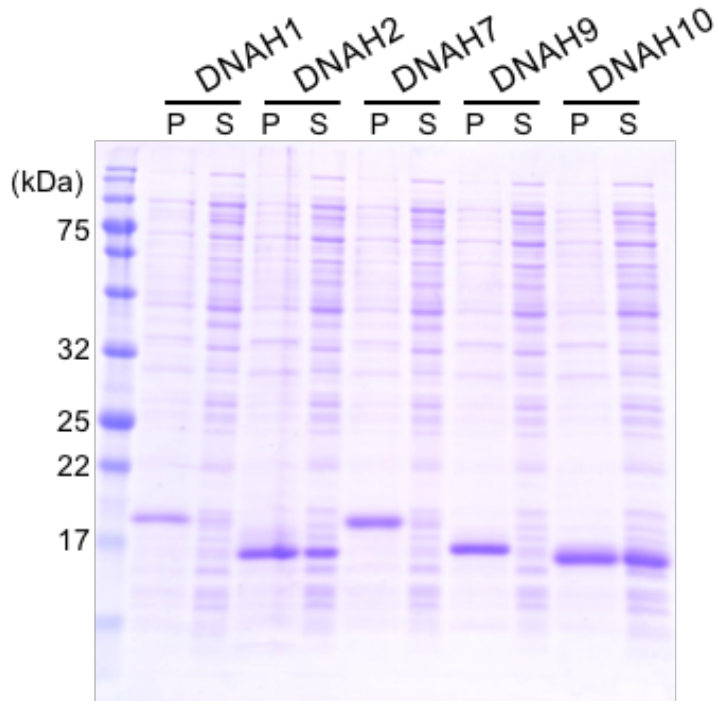


**Figure 4.1 Expression check of axonemal MTBDs**

(P) Precipitant fraction

(S) Supernatant fraction

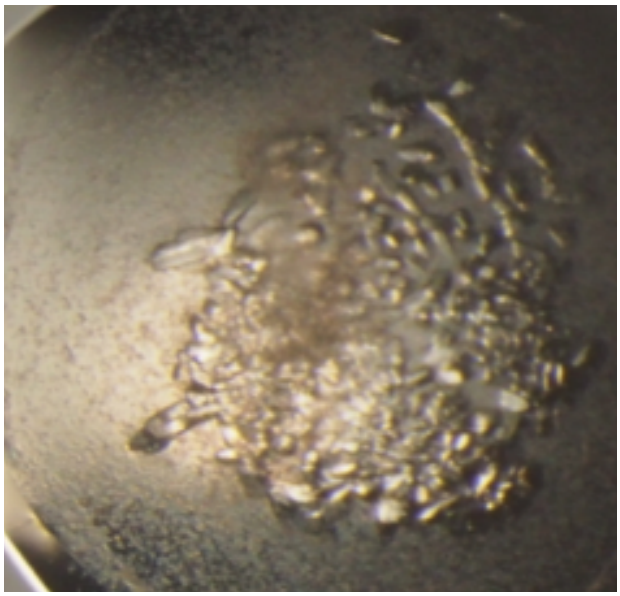

**Figure 4.2 Crystals of DNAH10 MTBD**

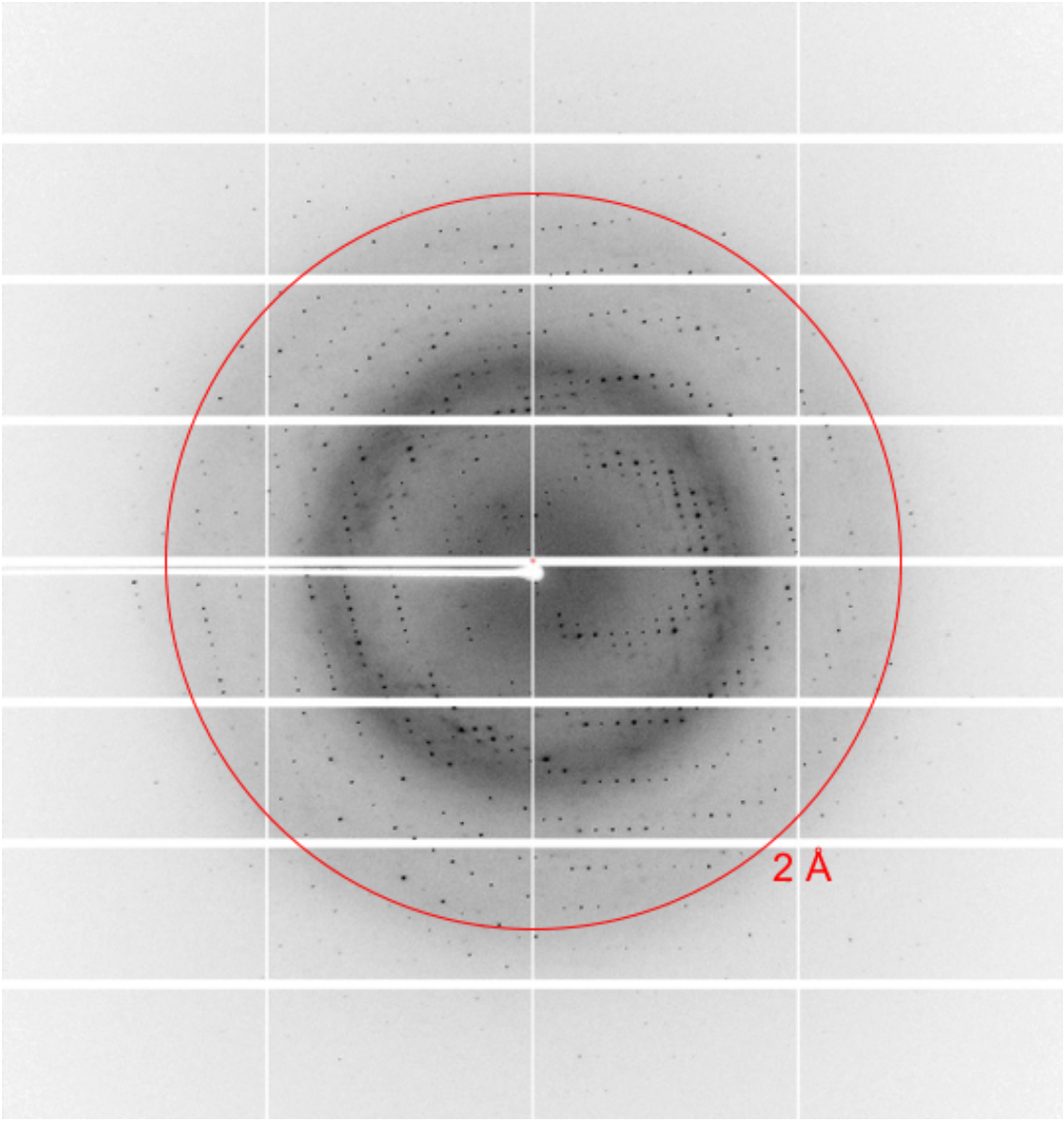


**Figure 4.3 X-ray diffraction image of crystal of DNAH10 MTBD**

**Table 4.1 Crystallographic data and refinement statistics of DNAH10 MTBD**

| | Se-Met data | Native data |
|---|---|---|
| ***Data collection*** | | |
| X-ray source | SPring-8 BL44XU | SPring-8 BL44XU |
| Wavelength (Å) | 0.9793 | 0.90000 |
| Space group | *P*1 | *P*1 |
| Unit cell parameters (Å) | | |
| *a, b, c* (Å) | 44.77, 47.93, 62.19 | 44.38, 47.80, 62.07 |
| α, β, γ (°) | 78.22, 78.98, 80.35 | 78.18, 79.01, 80.47 |
| Resolution (Å) | 46.50-1.80 (1.90-1.80) | 43.20-1.50 (1.59-1.50) |
| Completeness (%) | 95.4 (93.8) | 95.3 (93.9) |
| Redundancy | 3.5 (3.5) | 3.6 (3.7) |
| $R_{merge}$[1] (%) | 8.4 (96.0) | 4.8 (71.5) |
| $\langle I/\sigma(I) \rangle$ | 9.1 (1.2) | 12.1 (1.5) |
| CC1/2 | 99.6 (59.8) | 99.8 (89.4) |
| ***Refinement*** | | |
| Resolution (Å) | | 43.20-1.50 |
| $R_{work}$[2]/$R_{free}$[3] (%) | | 18.52/21.93 |
| Overall mean *B*-factor (Å$^2$) | | 40.77 |
| Ramachandran plot (%)[4] | | |
| Favored (%) | | 99.20 |
| Allowed (%) | | 0.60 |
| Outliers (%) | | 0.20 |
| r.m.s.d., bonds (Å) | | 0.009 |
| r.m.s.d., angles (°) | | 1.070 |

Values in parentheses are for the highest resolution shell.

[1] $R_{merge} = \sum_{hkl} \sum_i |I_i(hkl) - \langle I(hkl) \rangle| / \sum_{hkl} \sum_i I_i(hkl)$.

[2] $R_{work} = \sum_{hkl} \big||F_{obs}| - |F_{calc}|\big| / \sum_{hkl} |F_{obs}|$.[3] $R_{free}$ is the cross-validation R factor for the test set (5%) of reflections omitted from model refinement.

[4] Calculated by using MolProbity

### 4.3.2 Structure of DNAH10 MTBD

The asymmetric unit contained four DNAH10 MTBD molecules (Figure 4.4). All four molecules displayed similar conformations as that of known MTBD structures such as that of OADγ. However, I found the major difference between them in the position of the H6 helix which connects the H5 helix and CC2. In the C and D molecules, the H6 helix is a short helix as similar as in the other MTBDs (OADγ, dynein-c and DNAH7). In the A molecule, the H6 helix was no longer a helix but just a random coil, and in the B molecule the H6 helix was too flexible to build a model (Figure 4.4). Consequently, the RMSD values of Cα atoms of the position corresponding to the H6 helix between four molecules were very large (>4 Å) (Figure 4.5 and 4.6).

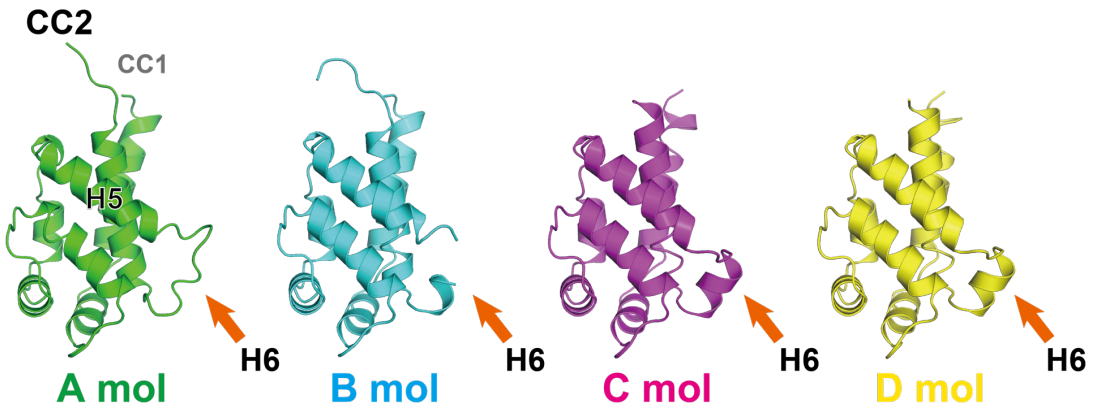


**Figure 4.4 Overall structures of DNAH10 MTBD**

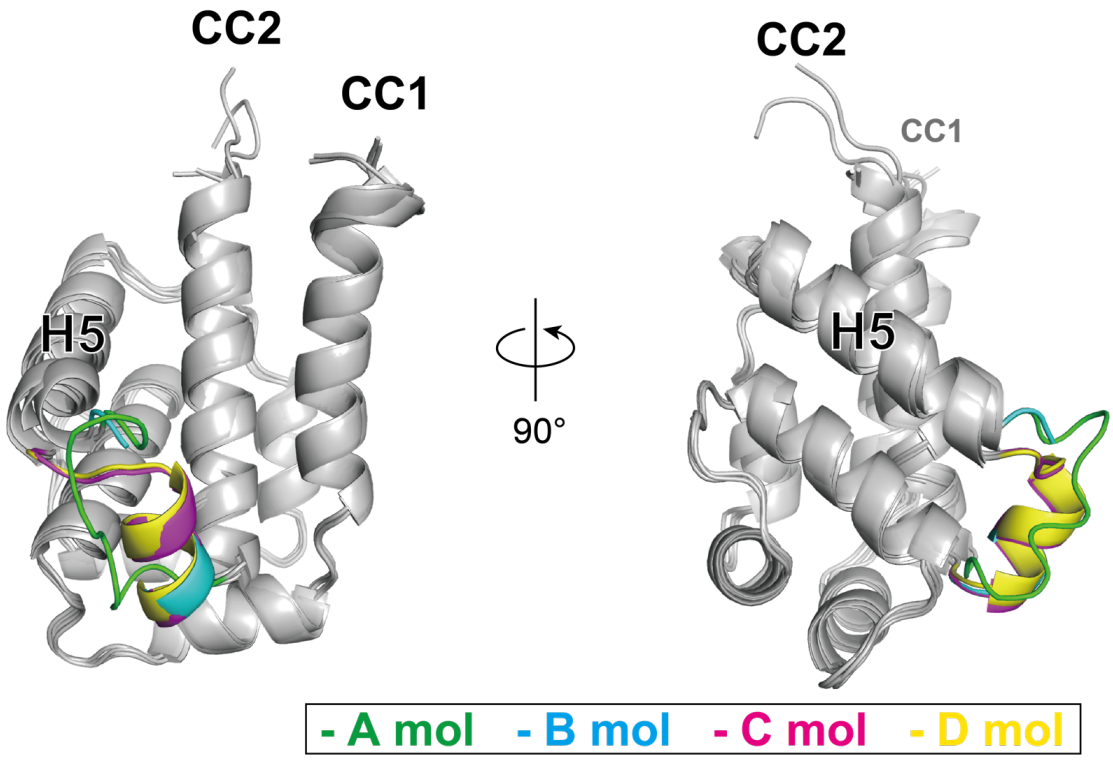


**Figure 4.5 Structural differences of the H6 helix in the DNAH10 MTBDs**

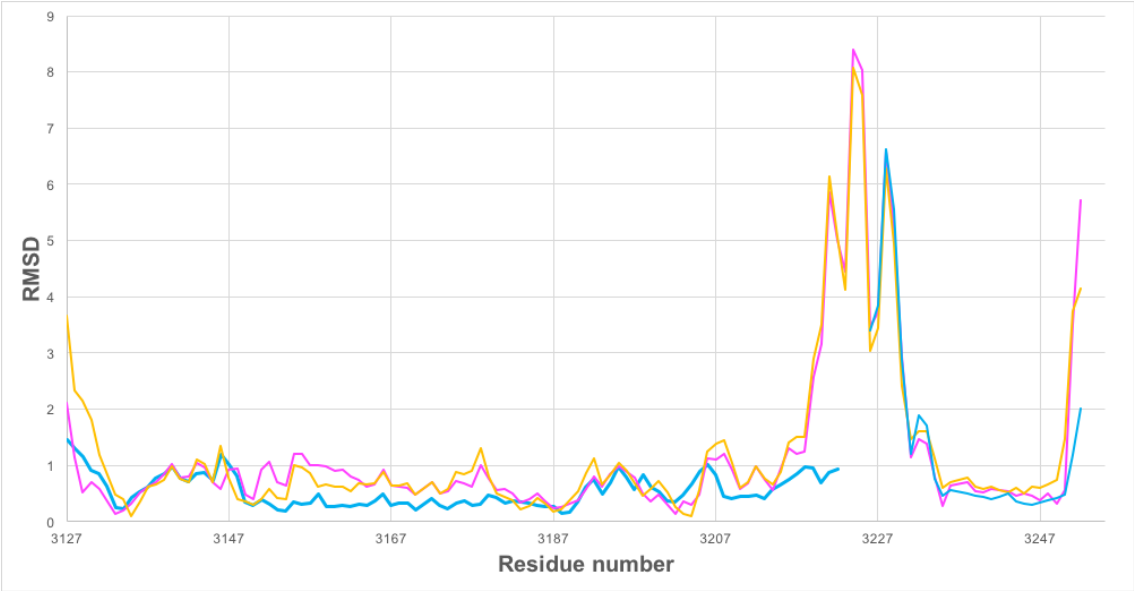


**Figure 4.6 The RMSD plot of Cα atoms between the A and other molecules**

The RMDS values for Molecule B, C and D are colored in cyan, magenta and yellow.

To confirm the structural flexibility of the H6 helix, I compared the b-factors of Cα atoms in A, B, C, and D molecules (Figure 4.7). The values of b-factures in the H6 helix were remarkably high in all four molecules. These results suggest that the conformational differences of the position of the H6 helix were caused by its intrinsic flexibility.

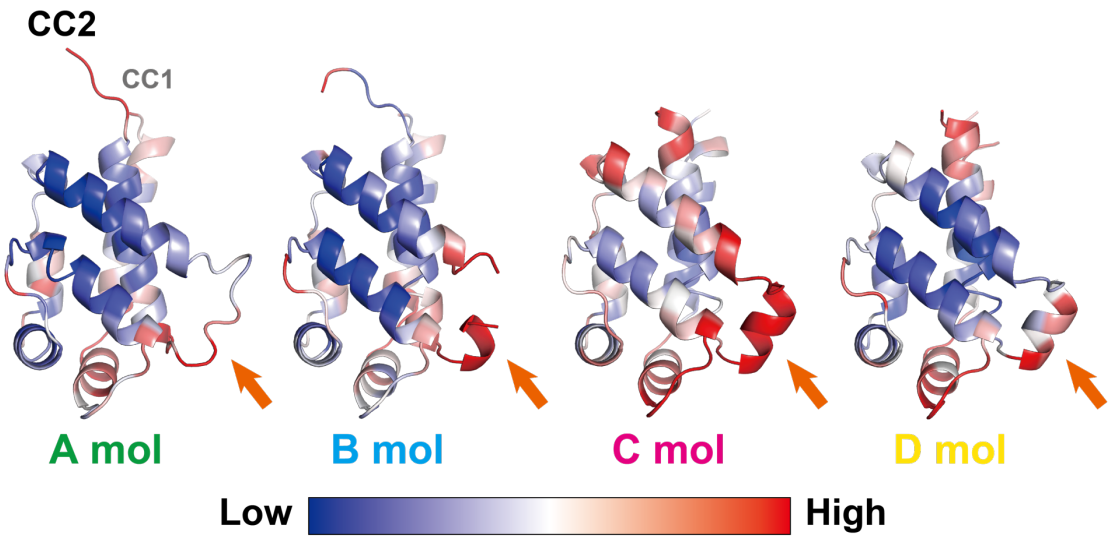


**Figure 4.7 Temperature factor representation of DNAH10 MTBD**

The temperature factors of Cα atom are colored blue-white-red corresponding to the low to high values. The orange arrows show positions of H6 helix.

Next, I compared the structure of DNAH10 MTBD with other known MTBD structures (Figure 4.8). The RMSDs of Cα atoms between the A molecule of DNAH10 MTBD and OADγ-MTBD (β-registry, LC1-bound form), dynein-c (β-registry), or DNAH7 MTBD (α-registry, the microtubule-bound form) were 1.72 Å, 2.34 Å, or 1.81 Å, respectively. Even using the C molecule of DNAH10 MTBD most different from the A molecule, the RMSD value was 2.0 Å against the microtubule bound DNAH7 (α-registry), which showed the strong similarity in 3D structure in the secondary structure level.

Moreover, I investigated whether the intrinsic flexibility of the H6 helix observed in DNAH10 MTBD are conserved in other axonemal and cytoplasmic dyneins by comparing temperature factors. In DNAH10 MTBD, the mean value of the temperature factor of the H6 helix displayed relatively high value compared with that of a whole molecule (Table 4.2). However, those of OADγ MTBD bound to LC1 and stalk region of cytoplasmic dynein 1 showed almost same values than those of a whole molecule (Table 4.2). This result implies that the flexibility of the H6 helix is unique to DNAH10. The flexibility might contribute to generate wide diversity of motor properties of dyneins.

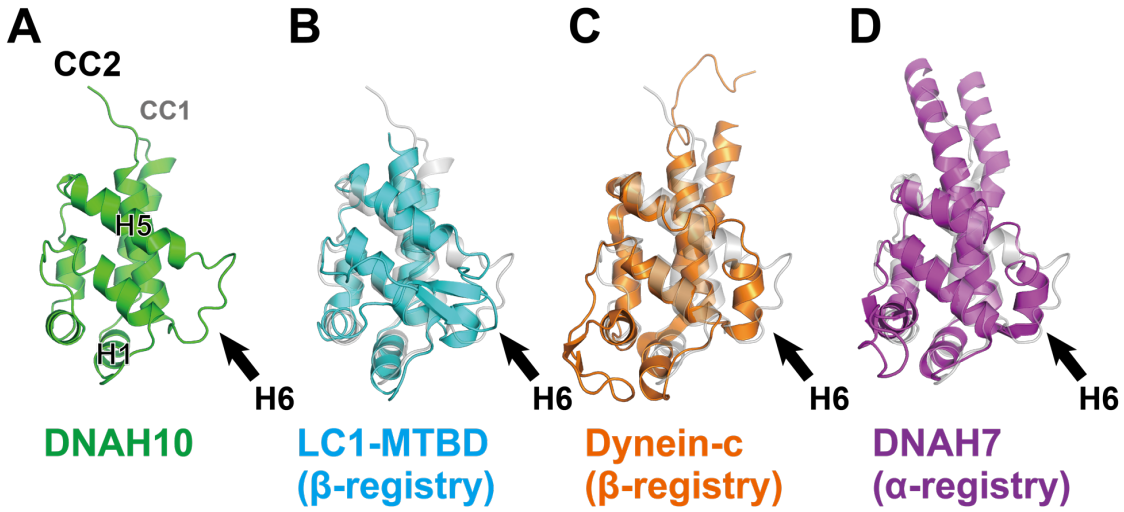


**Figure 4.8 Structural comparison of axonemal MTBDs**

The MTBD structure of DNAH10 (Left), that of OADγ bound to LC1 (PDB ID: 6L4P), that of dynein-c (PDB ID: 2RR7), and that of DNAH7 bound to the microtubule (PDB ID: 6RZA) are shown in green, cyan, orange, and magenta, respectively. The black arrows show the positions of H6 helix.

**Table 4.2 Comparison of temperature factor (Å$^2$) in the H6 helix**

| | All regions | H6 helix |
|---|---|---|
| DNAH10 | 40.56 | 51.49 |
| OADγ | 22.50 | 21.94 |
| Cytoplasmic dynein1 | 103.89 | 94.16 |

The mean values of temperature factor of MTBD and Stalk region are shown. The MTBD of DNAH10 except for B molecule, that of OADγ bound to LC1(PDB ID: 6L4P), and stalk region of cytoplasmic dynein 1 (PDB ID: 5AYH) are shown.

## 3.4 Discussion

I have determined the X-ray structure of DNAH10 MTBD at 1.50 Å resolution. Based on comparison with the other MTBD structures available in the Protein Data Bank, the three-dimensional structure of MTBD of DNAH10 is quite similar to that of OADγ, dynein-c excluding a flap region, and DNAH7. Although the whole structure of DNAH10 MTBD is quite similar to the others, the peripheral part corresponding to the H6 helix is somehow different from the others.

In the crystallographic asymmetric unit of this structure, there are four MTBD molecules, named A to D. In the C and D molecules, the H6 helix is a short helix as similar as in the other MTBDs (OADγ, dynein-c and DNAH7). But in the A molecule, the H6 helix was no longer a helix but just a random coil, and in the B molecule the H6 helix was too flexible to build a model (Figure 4.4). Since all four independent molecules showed exactly a same tendency of structural flexibility in one specific region, I think that this is due to not a crystal packing effect but an intrinsic molecular property.

If the binding mode of MTBD of DNAH10 is similar as that of other dyneins' MTBD, the H6 helix region of the MTBD is supposed to located at the interface to the microtubule. A flexible periphery of MTBD may become an adjustable finger or sticky shoe sole of specific IAD, because the temperature factors in the H6 helix of OADγ and cytoplasmic dynein 1 were approximately equal to those of other regions (Table 4.2). As I discussed the functional role of a flap of OADγ in chapter 3, this kind of additional flexible parts may contribute to tuning its affinity to the microtubule. Our model may be supported by a hypothetical modeling of IAD (DNAH10) MTBD-microtubule structure,

but further studies will be required to confirm both our structural model of the microtubule binding *in vitro* and the effect to ciliary/flagellar beating *in vivo*.

# Chapter 5

# Conclusion

Dynein motors are biologically important bio-nanomachines. Many atomic resolution structures of dynein components from different organisms have been analyzed by X-ray crystallography, cryo-EM and NMR spectroscopy. Here, I focused on the structures of axonemal dyneins especially on the stalk/MTBD region and performed three related structural works.

In Chapter 2, I revealed that the N- and C-terminal regions of LC1 are flexible enough to change their structures in secondary structure level and the conformational flexibility of LC1 is derived from its intrinsic property. It is concluded that the conformational changes in the N- and C-terminal regions of LC1 is physiologically important and may contribute to the interaction with the OADγ HC or the microtubule.

In Chapter 3, I revealed the complex structure of LC1 bound to the MTBD of OADγ by X-ray crystallography and identified two interaction sites of MTBD for LC1, the H5 helix and the flap region. Surprisingly, this structural analysis indicated that LC1 is not able to bind directly to the microtubule track in its current binding geometry. Then, I focused on the clear structural difference in the MTBD flap region between my complex structure and the dynein-c structure (Figure 3.11 B) to discuss the structural basis for the regulatory function of LC1. I found that the interaction sites in the flap region of OADγ are in principle not conserved based on the amino acids sequence alignments, suggesting that the interaction of LC1 with the H5 helix is physiologically dominant while that with

the flap region is relatively minor. Thus, I proposed that the flap released from the MTBD, in certain condition, might be able to bind to the adjacent protofilament in the same manner of DNAH7 (Figure 3.15), which may be related to a remote regulatory mechanism of LC1 (Figure 3.19).

In Chapter 4, I have determined the X-ray structure of DNAH10 MTBD at 1.50 Å resolution. Although the whole structure of DNAH10 MTBD is quite similar to the others, I found that the peripheral part corresponding to the H6 helix is somehow different from the others in its structural flexibility. If the binding mode of MTBD of DNAH10 is similar to that of other dyneins' MTBD, the H6 helix region of the MTBD is supposed to located at the interface to the microtubule. A flexible periphery of MTBD may become an adjustable part of specific IAD for microtubule binding. As I discussed the functional role of a flap of OADγ in chapter 3, this kind of additional flexible parts may contribute to tuning its affinity to the microtubule.

In parallel with recent developments in structural biology, such as cryo-electron tomography (cryo-ET) and single-particle cryo-EM analysis, more fascinating three-dimensional structures of dynein have become available. Based on these structures available in the Protein Data Bank, I would like to indicate two important viewpoints related to my PhD research.

One is the obvious imbalance in structural information between cytoplasmic and axonemal dynein. Atomistic structures are very much focused on cytoplasmic dyneins and remarkably less on axonemal dyneins. In contrast to the genes encoding cytoplasmic dynein HCs, those encoding axonemal dyneins are many and diverse. Each

axonemal dynein is likely to have a specific structural/functional role. However, the available atomistic structure of axonemal dynein is very limited. From that point of view, my research was aimed at expansion of structural information on axonemal dyneins. Actually, I have solved three X-ray structures of the LC1 alone and the LC1-MTBD (OADγ) from *Chlamydomonas reinhardtii* and the X-ray crystal structure of human DNAH10 (IAD) MTBD.

The second point is the resolution of structural information. This point is important because cryo-TEM or single particle cryo-EM often reported the middle range resolution structures and the less high-resolution. This is probably related to the physiological function of dynein molecules that walk along the MT by changing its structure in an ATPase dependent manner. I strongly believe that high-resolution X-ray structures of dynein's functional units give a big benefit to understand the precise functional role of dyneins. In fact, the resolution of my structures in this thesis is 1.55 Å (LC1), 1.70 Å (LC1-MTBD[OADγ]) and 1.50 Å, respectively. The high-resolution beyond 2.0 Å makes it possible to consider the anisotropic temperature factors, the number of hydrophobic/hydrophilic interactions, and the structural flexibility related to the temperature factors, which are important indications for intrinsic structural properties.

# References


1. Vale, R. D. (2003) The Molecular Motor Toolbox for Intracellular Transport. *Cell*. **112**, 467–480

2. Mallik, R., and Gross, S. P. (2004) Molecular Motors: Strategies to Get Along. *Curr. Biol.* **14**, R971–R982

3. Roberts, A. J., Kon, T., Knight, P. J., Sutoh, K., and Burgess, S. A. (2013) Functions and mechanics of dynein motor proteins. *Nat. Rev. Mol. Cell Biol.* **14**, 713–726

4. Bui, K. H., Sakakibara, H., Movassagh, T., Oiwa, K., and Ishikawa, T. (2008) Molecular architecture of inner dynein arms in situ in Chlamydomonas reinhardtii flagella. *J. Cell Biol.* **183**, 923–932

5. Pigino, G., Maheshwari, A., Bui, K. H., Shingyoji, C., Kamimura, S., and Ishikawa, T. (2012) Comparative structural analysis of eukaryotic flagella and cilia from Chlamydomonas, Tetrahymena, and sea urchins. *J. Struct. Biol.* **178**, 199–206

6. Burgess, S. A., Walker, M. L., Sakakibara, H., Knight, P. J., and Oiwa, K. (2003) Dynein structure and power stroke. *Nature*. **421**, 715–718

7. Carter, A. P., Cho, C., Jin, L., and Vale, R. D. (2011) Crystal Structure of the Dynein Motor Domain. *Science (80-. ).* **331**, 1159–1165

8. Kon, T., Sutoh, K., and Kurisu, G. (2011) X-ray structure of a functional full-length dynein motor domain. *Nat. Struct. Mol. Biol.* **18**, 638–642

9. Kon, T., Oyama, T., Shimo-Kon, R., Imamula, K., Shima, T., Sutoh, K., and Kurisu, G. (2012) The 2.8 Å crystal structure of the dynein motor domain. *Nature*. **484**, 345–350

10. Schmidt, H., Gleave, E. S., and Carter, A. P. (2012) Insights into dynein motor domain function from a 3.3-Å crystal structure. *Nat. Struct. Mol. Biol.* **19**, 492–497

11. Schmidt, H., Zalyte, R., Urnavicius, L., and Carter, A. P. (2014) Structure of human cytoplasmic dynein-2 primed for its power stroke. *Nature*. **518**, 435–438

12. Bhabha, G., Cheng, H. C., Zhang, N., Moeller, A., Liao, M., Speir, J. A., Cheng,

Y., and Vale, R. D. (2014) Allosteric communication in the dynein motor domain. *Cell*. **159**, 857–868

13. Zhang, K., Foster, H. E., Rondelet, A., Lacey, S. E., Bahi-Buisson, N., Bird, A. W., and Carter, A. P. (2017) Cryo-EM Reveals How Human Cytoplasmic Dynein Is Auto-inhibited and Activated. *Cell*. **169**, 1303-1314.e18

14. Kato, Y. S., Yagi, T., Harris, S. A., Ohki, S. Y., Yura, K., Shimizu, Y., Honda, S., Kamiya, R., Burgess, S. A., and Tanokura, M. (2014) Structure of the Microtubule-Binding Domain of Flagellar Dynein. *Structure*. **22**, 1628–1638

15. Lacey, S. E., He, S., Scheres, S. H., and Carter, A. P. (2019) Cryo-EM of dynein microtubule-binding domains shows how an axonemal dynein distorts the microtubule. *Elife*. 10.7554/eLife.47145

16. Gibbons, I. R., Garbarino, J. E., Tan, C. E., Reck-Peterson, S. L., Vale, R. D., and Carter, A. P. (2005) The affinity of the dynein microtubule-binding domain is modulated by the conformation of its coiled-coil stalk. *J. Biol. Chem.* **280**, 23960–23965

17. Kon, T., Imamula, K., Roberts, A. J., Ohkura, R., Knight, P. J., Gibbons, I. R., Burgess, S. A., and Sutoh, K. (2009) Helix sliding in the stalk coiled coil of

dynein couples ATPase and microtubule binding. *Nat. Struct. Mol. Biol.* **16**, 325–333

18. Nishikawa, Y., Inatomi, M., Iwasaki, H., and Kurisu, G. (2016) Structural Change in the Dynein Stalk Region Associated with Two Different Affinities for the Microtubule. *J. Mol. Biol.* **428**, 1886–1896

19. Redwine, W. B., Hernandez-Lopez, R., Zou, S., Huang, J., Reck-Peterson, S. L., and Leschziner, A. E. (2012) Structural Basis for Microtubule Binding and Release by Dynein. *Science (80-. ).* **337**, 1532–1536

20. Roberts, A. J., Numata, N., Walker, M. L., Kato, Y. S., Malkova, B., Kon, T., Ohkura, R., Arisaka, F., Knight, P. J., Sutoh, K., and Burgess, S. A. (2009) AAA+ Ring and Linker Swing Mechanism in the Dynein Motor. *Cell*. **136**, 485–495

21. Carter, A. P., Garbarino, J. E., Wilson-Kubalek, E. M., Shipley, W. E., Cho, C., Milligan, R. A., Vale, R. D., and Gibbons, I. R. (2008) Structure and Functional Role of Dynein's Microtubule-Binding Domain. *Science (80-. ).* **322**, 1691–1695

22. Höök, P., Mikami, A., Shafer, B., Chait, B. T., Rosenfeld, S. S., and Vallee, R. B. (2005) Long Range Allosteric Control of Cytoplasmic Dynein ATPase Activity

by the Stalk and C-terminal Domains. *J. Biol. Chem.* **280**, 33045–33054

23. Kon, T., Mogami, T., Ohkura, R., Nishiura, M., and Sutoh, K. (2005) ATP hydrolysis cycle–dependent tail motions in cytoplasmic dynein. *Nat. Struct. Mol. Biol.* **12**, 513–519

24. Schmidt, H., and Carter, A. P. (2016) Review: Structure and mechanism of the dynein motor ATPase. *Biopolymers*. **105**, 557–567

25. Carter, A. P. (2013) Crystal clear insights into how the dynein motor moves. *J. Cell Sci.* **126**, 705–713

26. Kikushima, K., and Kamiya, R. (2008) Clockwise Translocation of Microtubules by Flagellar Inner-Arm Dyneins In Vitro. *Biophys. J.* **94**, 4014–4019

27. Yamaguchi, S., Saito, K., Sutoh, M., Nishizaka, T., Toyoshima, Y. Y., and Yajima, J. (2015) Torque generation by axonemal outer-arm dynein. *Biophys. J.* **108**, 872–879

28. Grotjahn, D. A., and Lander, G. C. (2019) Setting the dynein motor in motion: New insights from electron tomography. *J. Biol. Chem.* **294**, 13202–13217

29. Bui, K. H., Sakakibara, H., Movassagh, T., Oiwa, K., and Ishikawa, T. (2008) Molecular architecture of inner dynein arms in situ in Chlamydomonas reinhardtii flagella. *J. Cell Biol.* **183**, 923–932

30. Lin, J., and Nicastro, D. (2018) Asymmetric distribution and spatial switching of dynein activity generates ciliary motility. *Science (80-. ).* **360**, eaar1968

31. Brokaw, C. J. (1994) Control of flagellar bending: A new agenda based on dynein diversity. *Cell Motil. Cytoskeleton*. **28**, 199–204

32. Goodenough, U., and Heuser, J. (1984) Structural comparison of purified dynein proteins with in situ dynein arms. *J. Mol. Biol.* **180**, 1083–1118

33. Toyoshima, Y. Y. (1987) Chymotryptic digestion of Tetrahymena 22S dynein. I. Decomposition of three-headed 22S dynein to one- and two-headed particles. *J. Cell Biol.* **105**, 887–895

34. Hornef, N., Olbrich, H., Horvath, J., Zariwala, M. A., Fliegauf, M., Loges, N. T., Wildhaber, J., Noone, P. G., Kennedy, M., Antonarakis, S. E., Blouin, J. L., Bartoloni, L., Nüsslein, T., Ahrens, P., Griese, M., Kuhl, H., Sudbrak, R., Knowles, M. R., Reinhardt, R., and Omran, H. (2006) DNAH5 mutations are a common cause of primary ciliary dyskinesia with outer dynein arm defects. *Am.*

*J. Respir. Crit. Care Med.* **174**, 120–126

35. King, S. M., and Patel-King, R. S. (2012) Functional architecture of the outer arm dynein conformational switch. *J. Biol. Chem.* **287**, 3108–3122

36. Benashski, S. E., Patel-King, R. S., and King, S. M. (1999) Light chain 1 from the Chlamydomonas outer dynein arm is a leucine-rich repeat protein associated with the motor domain of the gamma heavy chain. *Biochemistry*. **38**, 7253–64

37. Ichikawa, M., Saito, K., Yanagisawa, H., Yagi, T., Kamiya, R., Yamaguchi, S., Yajima, J., Kushida, Y., Nakano, K., Numata, O., and Toyoshima, Y. Y. (2015) Axonemal dynein light chain-1 locates at the microtubule-binding domain of the γ heavy chain. *Mol. Biol. Cell*. **26**, 4236–4247

38. Patel-King, R. S., and King, S. M. (2009) An outer arm dynein light chain acts in a conformational switch for flagellar motility. *J. Cell Biol.* **186**, 283–295

39. Rompolas, P., Patel-King, R. S., and King, S. M. (2010) An outer arm Dynein conformational switch is required for metachronal synchrony of motile cilia in planaria. *Mol. Biol. Cell*. **21**, 3669–79

40. Mazor, M., Alkrinawi, S., Chalifa-Caspi, V., Manor, E., Sheffield, V. C.,

Aviram, M., and Parvari, R. (2011) Primary ciliary dyskinesia caused by homozygous mutation in DNAL1, encoding dynein light chain 1. *Am. J. Hum. Genet.* **88**, 599–607

41. Horváth, J., Fliegauf, M., Olbrich, H., Kispert, A., King, S. M., Mitchison, H., Zariwala, M. A., Knowles, M. R., Sudbrak, R., Fekete, G., Neesen, J., Reinhardt, R., and Omran, H. (2005) Identification and analysis of axonemal dynein light chain 1 in primary ciliary dyskinesia patients. *Am. J. Respir. Cell Mol. Biol.* **33**, 41–47

42. Mullen, G. P., King, S. M., Wu, H., Maciejewski, M. W., Marintchev, A., and Benashski, S. E. (2000) Solution structure of a dynein motor domain associated light chain. *Nat. Struct. Biol.* **7**, 575–579

43. Wu, H., Blackledge, M., Maciejewski, M. W., Mullen, G. P., and King, S. M. (2003) Relaxation-based structure refinement and backbone molecular dynamics of the dynein motor domain-associated light chain. *Biochemistry*. **42**, 57–71

44. Otwinowski, Z., and Minor, W. (1997) Processing of X-ray diffraction data collected in oscillation mode. *Methods Enzymol.* **276**, 307–326

45. Long, F., Vagin, A. A., Young, P., and Murshudov, G. N. (2008) BALBES : a

molecular-replacement pipeline. *Acta Crystallogr. Sect. D Biol. Crystallogr.* **64**, 125–132

46. Emsley, P., Lohkamp, B., Scott, W. G., and Cowtan, K. (2010) Features and development of Coot. *Acta Crystallogr. Sect. D Biol. Crystallogr.* **66**, 486–501

47. Painter, J., and Merritt, E. A. (2006) TLSMD web server for the generation of multi-group TLS models. *J. Appl. Crystallogr.* **39**, 109–111

48. Lovell, S. C., Davis, I. W., Arendall, W. B., de Bakker, P. I. W., Word, J. M., Prisant, M. G., Richardson, J. S., and Richardson, D. C. (2003) Structure validation by Calpha geometry: phi,psi and Cbeta deviation. *Proteins*. **50**, 437–450

49. Heinig, M., and Frishman, D. (2004) STRIDE: a web server for secondary structure assignment from known atomic coordinates of proteins. *Nucleic Acids Res.* **32**, W500–W502

50. Yang, J., Xu, C., Wang, C., and Kopeček, J. (2006) Refolding Hydrogels Self-Assembled from N -(2-Hydroxypropyl)methacrylamide Graft Copolymers by Antiparallel Coiled-Coil Formation. *Biomacromolecules*. **7**, 1187–1195

51. Nair, R., Salvi, P., Banerjee, S., Raiker, V. A., Bandyopadhyay, S., Soorapaneni, S., Kotwal, P., and Padmanabhan, S. (2009) Yeast extract mediated autoinduction of lacUV5 promoter: An insight. *N. Biotechnol.* **26**, 282–288

52. Adams, P. D., Grosse-Kunstleve, R. W., Hung, L.-W., Ioerger, T. R., McCoy, A. J., Moriarty, N. W., Read, R. J., Sacchettini, J. C., Sauter, N. K., and Terwilliger, T. C. (2002) PHENIX: building new software for automated crystallographic structure determination. *Acta Crystallogr. Sect. D Biol. Crystallogr.* **58**, 1948–1954

53. Toda, A., Tanaka, H., and Kurisu, G. (2018) Structural atlas of dynein motors at atomic resolution. *Biophys. Rev.* **10**, 677–686

54. Emsley, P., and Cowtan, K. (2004) Coot: Model-building tools for molecular graphics. *Acta Crystallogr. Sect. D Biol. Crystallogr.* **60**, 2126–2132

55. Laskowski, R. A., and Swindells, M. B. (2011) LigPlot+: Multiple Ligand–Protein Interaction Diagrams for Drug Discovery. *J. Chem. Inf. Model.* **51**, 2778–2786

56. Uchimura, S., Fujii, T., Takazaki, H., Ayukawa, R., Nishikawa, Y., Minoura, I., Hachikubo, Y., Kurisu, G., Sutoh, K., Kon, T., Namba, K., and Muto, E. (2015)

A flipped ion pair at the dynein-microtubule interface is critical for dynein motility and ATPase activation. *J. Cell Biol.* **208**, 211–222

57. Furuta, A., Amino, M., Yoshio, M., Oiwa, K., Kojima, H., and Furuta, K. (2016) Creating biomolecular motors based on dynein and actin-binding proteins. *Nat. Nanotechnol.* **12**, 233–237

58. Kabsch, W. (2010) Integration, scaling, space-group assignment and post-refinement. *Acta Crystallogr. Sect. D Biol. Crystallogr.* **66**, 133–144

59. Terwilliger, T. C., Adams, P. D., Read, R. J., McCoy, A. J., Moriarty, N. W., Grosse-Kunstleve, R. W., Afonine, P. V., Zwart, P. H., and Hung, L.-W. (2009) Decision-making in structure solution using Bayesian estimates of map quality: the PHENIX AutoSol wizard. *Acta Crystallogr. Sect. D Biol. Crystallogr.* **65**, 582–601

60. Afonine, P. V., Grosse-Kunstleve, R. W., Echols, N., Headd, J. J., Moriarty, N. W., Mustyakimov, M., Terwilliger, T. C., Urzhumtsev, A., Zwart, P. H., and Adams, P. D. (2012) Towards automated crystallographic structure refinement with phenix.refine. *Acta Crystallogr. Sect. D Biol. Crystallogr.* **68**, 352–367

61. Matthews, B. W. (1968) Solvent content of protein crystals. *J. Mol. Biol.* **33**,

491–497

# List of publications

1. Toda, A., Tanaka, H., and Kurisu, G. (2018) Structural atlas of dynein motors at atomic resolution. *Biophys. Rev.* **10**, 677–686

2. Toda, A., Nishikawa, Y., Tanaka, H., Yagi, T., and Kurisu, G. (2020) The complex of outer-arm dynein light chain-1 and the microtubule-binding domain of the γ heavy chain shows how axonemal dynein tunes ciliary beating. *Journal of Biological Chemistry*. (in revision)

3. Toda, A., Nishikawa, Y., Tanaka, H. and Kurisu, G. (2020) X-ray structure of the microtubule binding domain of the Inner Arm Dynein (DNAH10). (in preparation)